Mikko Ruoho

Nanostructured thermoelectric materials.

School of Electrical Engineering

Thesis submitted for examination for the degree of Master of Science in Technology.

Espoo 27.2.2012

Thesis supervisor and instructor:

Prof. Ilkka Tittonen

Aalto University
School of Electrical
Engineering

AALTO UNIVERSITY
SCHOOL OF ELECTRICAL ENGINEERING

ABSTRACT OF THE
MASTER'S THESIS

Author: Mikko Ruoho

Title: Nanostructured thermoelectric materials.

Date: 27.2.2012 Language: English Number of pages:7+41

Department of Micro and Nanosciences

Professorship: Physics of micro technologies Code: S-129

Supervisor and instructor: Prof. Ilkka Tittonen

Thermoelectric power generation has attracted growing interest during the last years due to the increasing need for renewable energy sources and to achieving a better energy conversion efficiency. Conversion of thermal energy to electricity may directly be done using semiconducting solid material, yet the efficiency is rather modest. However, the efficiency has been improved by more than a factor of two during last decades thanks to taking use of material engineering down to the nanoscale.

In this work, the literature part is divided into two sections. The first section reviews the most common thermoelectric materials. The second section describes the phenomena behind the thermoelectric conversion efficiency and discusses strategies to improve it.

The experimental part of this thesis is divided into the two parts. First, measurements of thermoelectric quantities, the Seebeck coefficient and resistivity are discussed and self-made measurement setup is introduced. Then ALD deposited thin films are studied with the setup.

ALD deposited ZnO was found to be very conductive in comparison to bulk material, yet the Seebeck coefficient was lower. In case of aluminum doped ZnO, the resistivity was of the same order as those of bulk material but the Seebeck coefficient was rather modest.

Keywords: Termoelectric, power generation, power factor, thermal conductivity, Seebeck coefficient, nanostructure, Zinc oxide

AALTO-YLIOPISTO
SÄHKÖTEKNIIKAN KORKEAKOULU

DIPLOMITYÖN
TIIVISTELMÄ

Tekijä: Mikko Ruoho

Työn nimi: Nanorakenteiset lämpösähköiset materiaalit

Päivämäärä: 27.2.2012 Kieli: Englanti Sivumäärä:7+41

Mikro- ja nanotekniikan laitos

Professuuri: Sähköfysiikka Koodi: S-129

Valvoja ja ohjaaja: Prof. Ilkka Tittonen

Kiinnostus lämpösähköiseen energian muuntamiseen on lisääntynyt huomattavasti viime vuosina uusiutuvien energialähteiden tarpeen lisääntyessä. Energiaa voidaan muuttaa lämmöstä sähköksi kiinteillä puolijohdemateriaaleilla, vaikka hyötysuhde jääkin vielä vaatimattomaksi. Viimeisimpien kymmenen vuoden aikana hyötysuhde on kuitenkin yli kaksinkertaistunut, kun on havaittu, että hyötysuhdetta voi parantaa nanorakenteisuudella.

Tämä opinnäytteen kirjallisuusosa on jaettu kahteen osaan. Ensimmäinen osa käy läpi yleisimmät lämpösähköiset materiaalit, niiden ominaisuudet ja mistä ominaisuudet johtuvat. Nykyinen ymmärrys lämpösähköisestä ilmiöstä perustuu näiden materiaalien tutkimuksessä kerättyyn tietoon. Toisessa osassa käsitellään ilmiöitä, joista muunnoksen hyötysuhde riippuu ja kuinka hyötysuhdetta voidaan parantaa. Kokeellinen osa koostuu myös kahdesta osasta. Ensimmäinen kertoo lämpösähköisien ominaisuuksien mittauksista ja esitelee itse rakennetun laitteen niiden mittaamiseksi. Toisessa osassa tutkitaan ALD kasvatettujen ohutkalvojen lämpösähköisiä ominausuuksia.

ALD kasvatuttu ZnO osoittautui hyvin sähköä johtavaksi verrattuna makroskooppisilla valmistusmetelmillä tehtyihin kappaleisiin, Seebeckin kertoimen arvon ollessa samaa luokkaa. Alumiinilla seostettu ZnO:n sähkönjohtavuus oli samaa luokkaa kuin makroskooppisilla valmistusmetelmillä tehtyillä kappaleilla, mutta Seebeckin kertoimen arvo jäi varsin vaatimattomaksi.

Avainsanat: Lämpösähkö, energianmuuntaminen, Seebeckin vakio, lämmönjohtavuus, resistiivisyys, nanorakenne, Sinkkioksidi

Preface

First I would like to acknowledge professor Ilkka Tittonen for the chance to work in this fascinating field.

I would also like to thank my colleagues Ville Pale, Mikhail Erdmanis and Osmo Vänskä for helping with text editor, Matlab, Comsol, troubleshooting the measurement device and just for making the working atmosphere great. Moreover, I would like to thank Dr. Nikolai Chekurov for teaching the usage of ALD and SEM. Tuomas Rossis previous work helped me a lot getting started in the lab, also I would like to thank him for helping with the measurement equipment.

I would like to acknowledge Dr. Cao Ming and Dr. Lassi Karvonen for introducing their labs and working methods and hence enabling the work done in this thesis. Escpecially I would like to thank Dr. Yi Ma, Dr. Daniel Cederkrantz and Richard Heijl for not only for showing their lab but also allowing me work there and even measuring some samples for me.

I would also like to acknowledge people at micronova whom with I have had the pleasure to work with and who have the showed me how to use the equipment needed for the work escpecially Sergei Novikov, Risto Salo, Esa Tuovinen, Jonne Koski, Alex Perros, Lasse Karvonen and Alex Kravchenko.

Our project collaborators at VTT and MIKES are acknowledged. Especially Dr. Jyrki Tervo has been actively looking collaboration and pushing me onward. Special thanks goes to Dr. Jaani Nissilä and Emma Mykkänen how have diligently worked on thermal conductivity measurement system which will play a key role for future work. Also Dr. Tomi Mattila is thanked for discussions and improvement ideas for the measurement device.

I would like to thank also my parents, Jukka and Helena, who have been supportive and interested in my work, at least whether it will be ever finished. Finally I would like to thank my girlfriend Hilma who has encouraged and supported me.

Göteborg, 24.2.2011

Mikko Ruoho

Contents

Symbols and abbreviations

Symbols

A	Acoustic impedance
C	Lattice heat capacity
CF	Crystal complexity factor, number of atoms per primitive unit cell
c_i	Speed of sound, longnitudal or transverse
C_λ	Spectral specific heat per unit wavelength
d_{pd}	Diameter of a point defect
e	Elementary charge
E_F	Fermi energy
F	Faraday's constant
$g(E)$	Electronic density of states (DOS)
k	Wave vector
k_B	Boltzmann constant
L	Lorenz number
l	Phonon mean free path
L_α	Cutoff mean-free path
n	Number of charge carriers
P	Electric power
q	Local heat flux density
q_L	Phonon wave vector
R	Electrical resistance
S	Absolute Seebeck coefficient
s	Partial molar entropy
S_{AB}	Differential Seebeck coefficient between elements a and b
T	Temperature
V	Voltage
v	Group velocity
v_p	the phonon velocity
Z	Thermoelectric figure-of-merit
χ	Compressibility
κ	Thermal conductivity
κ_e	Charge carrier thermal conductivity
κ_l	Lattice thermal conductivity
λ_{ph}	Phonon wavelength
μ	Charge carrier mobility
μ_T	Thomson heat
ω	Angular frequency
ρ	Electrical resistivity
ρ_d	Density
σ	Electrical conductivity
τ	Thomson coefficient

θ_{in}	the angle of incidence
$\hbar$	Reduced Plank constant

Abbreviations

ALD	Atomic Layer Deposition
TAGS	Alloy containing elements Te, Ag, Ge, and Sb
LAST	Alloy containing elements Pb, Ag, Sb, and Te
LASTT	Alloy containing elements Pb, Ag, Sn, Sb, and Te
SALT	Alloy containing elements Na, Sb, Pb, and Te
PGEC	Phonon-glass electron-crystal
DOS	Electronic density of states
TMA	Trimethylaluminium
DEZ	Diethylzinc

1 Introduction

Thermoelectric power generation is a solid state conversion process from thermal energy into electricity. Temperature gradient in a conductor generates an electric field in opposite direction in order to restore equilibrium [1]. Although the voltage difference between the hot and cold end of one piece of material cannot be directly measured, in a junction of pair of conductors at hot or cold temperature compared to the ambient, a small voltage can be measured. This phenomenon is called the Seebeck effect and is illustrated in Figure 1.1. The two conductors form a thermocouple generating typically voltages of tens of microvolts per degree of temperature difference. The induced voltage depends on the temperature difference and the conductors by

$$V = S_{AB}(T_1 - T_2), \tag{1.1}$$

where S_{AB} is the differential Seebeck coefficient between materials A and B, defined by $S_{AB} = V/\Delta T$. The phenomenon being reversible, it is possible to heat or cool the connected end by applying a voltage difference between the open ends. This is called the Peltier effect. [2, 3]

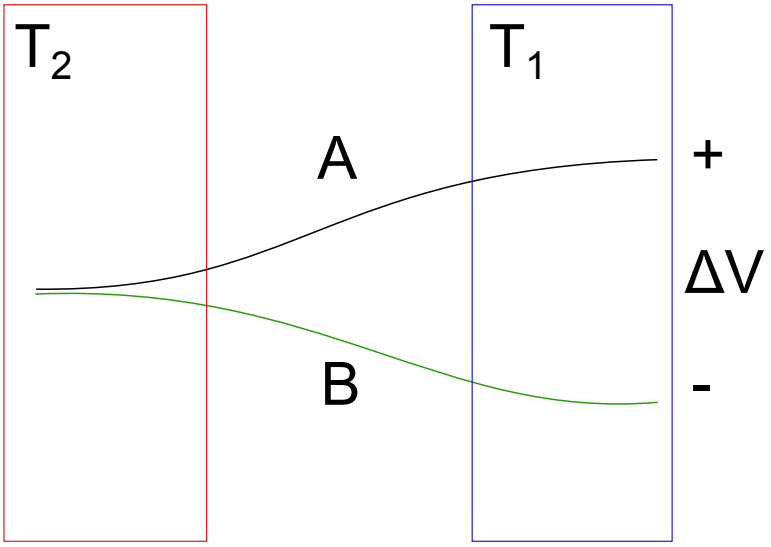

Figure 1.1: Voltage difference is generated by the Seebeck effect between open ends of conductors A and B, when they are connected at one point at different temperature from the open ends.

Although the absolute value of the Seebeck coefficient S cannot be directly measured, it can be determined with the help of superconductors since the value of S_{AB} for all pairs of superconductors is zero. Thus, when a conductor is connected with a superconductor, S_{AB} equals S. Obviously, this is possible only at low temperatures and the Thomson coefficient, τ, must be determined in order to find the value at higher temperatures. After measuring the Thomson coefficient, the absolute value of the Seebeck coefficient can be calculated using the Kelvin relation

$$\tau = T\frac{dS}{dT}, \tag{1.2}$$

where T is the absolute temperature. Most metals have very small values for absolute Seebeck coefficient and as a consequence, nearly all practical thermoelectric materials are semiconductors. [4]

Seebeck coefficient is also a measure for 'electronic entropy' i.e. entropy per charge carrier in a material [5]. The measure is to be regarded as transport entropy which might not be the same in isothermal conditions. Moreover, Seebeck coefficient might be the only practical means to obtain partial molar entropies of electrons in metals. The partial molar entropy

$$s = SF, \tag{1.3}$$

where F is Faraday's constant and S the absolute Seebeck coefficient.

A thermoelectric module consists of multiple thermocouples both n- and p-type thermoelectric legs connected in series. This is illustrated in Figure 1.2. The power generated by such a system is roughly estimated by,

$$P = N\frac{V^2}{R} = N\frac{S^2\Delta T^2}{R}, \tag{1.4}$$

where R is the electronic resistance of the whole circuit to which the module is connected and N the number of thermocouples in series. For a module with matched load the power is

$$P = N\frac{S^2\Delta T^2\sigma A}{2h}, \tag{1.5}$$

where h is the height of a thermocouple leg, A is the cross-sectional area of a thermocouple leg and σ is the electrical conductivity. The denominator of 2 comes from the contribution of the load circuit. From this formula we see that the material properties that determine the power generated by a thermoelectric generator are the Seebeck coefficient and electrical conductivity. $S^2\sigma$ is often referred as the electrical

power factor. As Fourier's law of thermal conduction shows, the local heat flux density q $= -\kappa A \Delta T/h$ and we get

$$P = N \frac{S^2 q^2 \sigma}{2\kappa^2}, \tag{1.6}$$

where κ is the thermal conductivity. Thermal conductivity determines how large heat flux is needed in order to sustain a certain temperature difference.

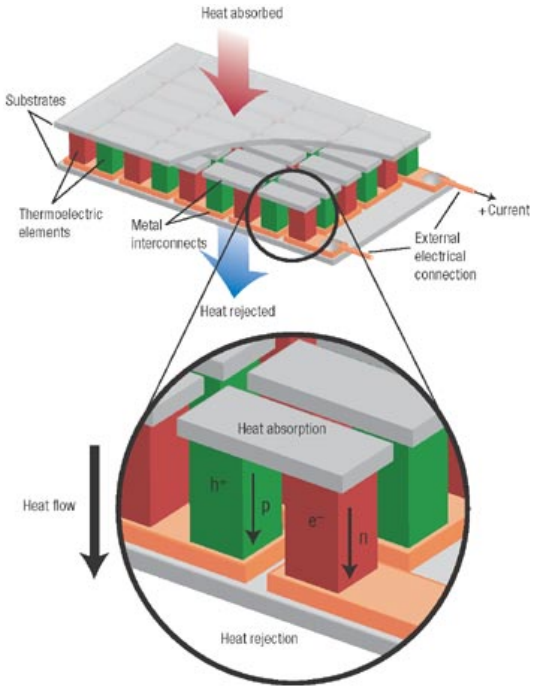

Figure 1.2: Thermoelectric module. [6]

The performance of a thermoelectric device is given by the dimensionless figure-of-merit

$$Z = \frac{S^2 \sigma}{\kappa}. \tag{1.7}$$

It is assumed that the two arms of the thermocouple have similar material constants. Z does not take into account that all material parameters are temperature dependent, thus often Z is multiplied with absolute temperature. Thermocouple having an average figure of merit of about one would have a conversion efficiency of about 10 % when operated with the temperature difference of 250 K. [3]

The use of ZT is, however, also controversial. ZT has been criticized to neglect certain aspects; it is only a measure of heat conversion rate i.e. efficiency. Maximum power generated for a certain power factor is actually achieved by maximizing

thermal conductivity and accepting low conversion efficiency [7]. Moreover, the determination of ZT requires large amount of work in preparation of specimen at various doping levels as well as measurements of κ, α and σ over a wide temperature range. Therefore, S-ln σ plot has been proposed as an optimization tool for power factor [8]. Despite the criticism, no real generally accepted alternative for ZT has been proposed.

In order to engineer thermoelectrics, one has to either increase electrical conductivity or decrease thermal conductivity. However, they are interconnected by charge carrier concentration given by the Wiedemann-Franz law

$$\kappa_e = L\sigma T = ne\mu LT, \tag{1.8}$$

where the Lorenz number is

$$L = \frac{\pi^2}{3}\left(\frac{k_B}{e}\right)^2 \tag{1.9}$$

and μ is the charge carrier mobility. It is worth noting that the Lorenz number is constant only for metals. Thermal conductivity in thermoelectrics arises from two factors that are thermal conductivity by charge carriers, κ_e, and thermal conductivity by lattice phonons, κ_l. [6] The Wiedemann-Franz law applies only to thermal conductivity by charge carriers, which is about 1/3 of total electrical conductivity in thermoelectric materials. In contrast, the value of Seebeck coefficient decreases as a function of the carrier concentration. As a result, semiconductors are the material of choice for thermoelectrics. This is illustrated in Figure 1.3. [3]

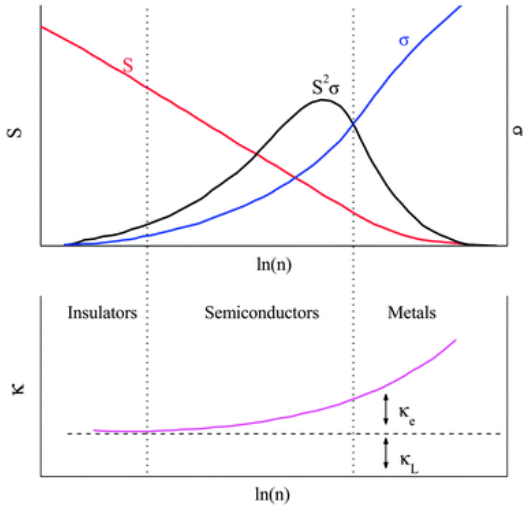

Figure 1.3: Dependency of Seebeck coefficient (S), electrical conductivity (σ), power factor($S^2\sigma$) and thermal conductivity(κ) on the concentration of charge carriers. [9]

2 Thermoelectric materials

The state of the art material for thermoelectric applications in commercial devices is still Bi_2Te_3 with ZT ≈ 1 that was discovered in 1950's [10]. It is a semiconductor with an indirect band gap of about 0.15 eV [11]. The conduction and valence bands have both six valleys, which is illustrated in Figure 2.1. It can be alloyed with Sb for p-type and with Se for n-type material. The alloying is typically done before material is grown, i.e. in liquid solution at high temperature. Material may be fabricated by controlled cooling and crystal growth or the other alternative is to cool the liquid solution, grind and sinter the particles at a temperature of about 500 ^{o}C and pressure of 10^5 - 10^6 kPa. The atomic structure of Bi_2Te_3 consists of five layers of atoms $Te^{[1]}$ - Bi - $Te^{[2]}$ - Bi - $Te^{[1]}$, which is repeated. This is illustrated in Figure 2.2. The layers are held together by van der Vaals interactions. For this reason, Bi_2Te_3 crystals can be easily cleaved along the layers. Moreover, impurity atoms, such as copper, can readily occupy interstitial sites between weakly and loosely bounded $Te^{[1]}$ layers as well as move easily from one site to another. The diffusion coefficient of copper as well as electronic transport properties, Hall coefficient and magneto resistance are, obviously, orientation dependent. However, the Seebeck coefficient of doped Bi_2Te_3 is independent of orientation. In the undoped case, the Seebeck coefficient depends on the direction of the temperature gradient. [12]

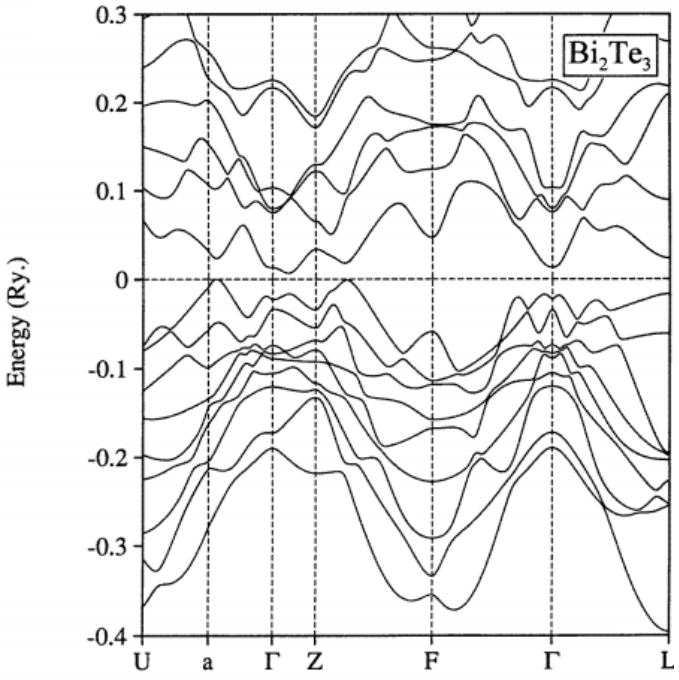

Figure 2.1: Calculated electronic band structure for bismuth telluride [13].

Recently, nanostructuring of Bi_2Te_3 has raised ZT. The controversial [11] record ZT of 2.4 at room temperature was a superlattice of Bi_2Te_3 and Sb_2Te_3 grown by low-temperature metal-organic chemical vapour deposition. The high ZT value was

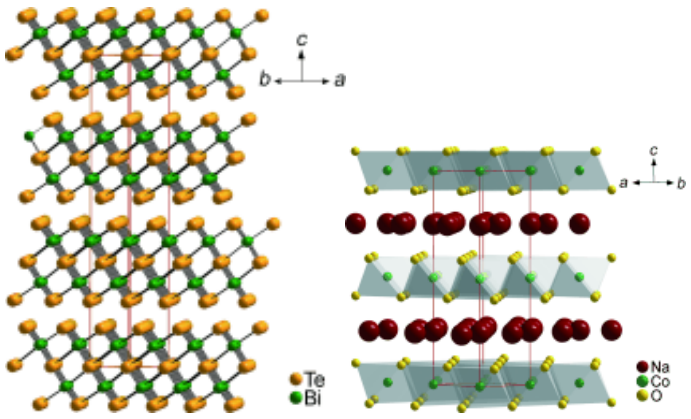

(a) Bi_2Te_3 (b) $NaCo_2O_4$

Figure 2.2: Layered crystal structures of a) Bi_2Te_3 and b) $NaCo_2O_4$. In Bi_2Te_3 layers of five atoms are stacked by van der Waals interactions. In $NaCo_2O_4$ Na^+ ions occupy half of the atomic sites between $[CoO_2]^-$ layers. [11]

achieved in the direction perpendicular to the Bi_2Te_3 layers. The 1 - 5 nm thick superlattice layers had remarkably low thermal conductivity of 0.24 W m^{-1} K^{-1} and cross-plane electron mobility, unlike bulk Bi_2Te_3, comparable to in-plane mobility. The decrease in thermal conductivity was proposed to arise from mirror like phonon back reflection. The explanation for the similarity of the mobilities is based on very small band cap of the superlattice layers. [14] The band offset is supposed to be smaller than average thermal energy of charge carrier, hence having negligible influence on the cross-plane electrical transport, yet efficiently reducing thermal transport by limiting the phonon mean free path. However, as this is the case also for bulk Bi_2Te_3, is the conclusion questionable. Neither has anyone been able to reproduce the result. [11].

PbTe arranges as the NaCl, face-centred cubic, crystal structure, causing isotropic material properties. With a band gap of 0.32 eV, it can be either n- or p-type depending on the stoichiometry. It may also be doped in order to modify its transport properties; Na, Au, Ti, and O act as acceptors and Zn, Cd, In, Bi, and Cl as donors. With a maximum ZT slightly under unity at 650 K, PbTe is the material of choice in the temperature range of 600 - 800 K [11]. For practical applications PbTe is alloyed by substituting tin for lead and sulphur or selenium for Telluride. [4, 15]

Alloys containing elements Te, Ag, Ge, and Sb, mainly between the compounds $AgSbTe_2$ and GeTe, are often referred as TAGS. These alloys are closely related to PbTe since part of the solid solution range has the same face-centred cubic crystal structure. They are intrinsically p-type materials and are typically combined with PbTe n-type leg [11]. These compounds have significantly lower lattice thermal conductivity than PbTe and are able to achieve ZT above unity. The crystal structure will transform into rhombohedral, when concentration of GeTe is less than 80%. Interestingly, at this point the highest ZT is achieved; lattice strain is believed to reduce the thermal conductivity. However, this will happen at the expend of

mechanical properties. [12]

Combination of $AgSbTe_2$ and PbTe, $AgPb_mSbTe_{2+m}$ is known as LAST-m family (lead antimony silver telluride). These materials are stable up to 1200 K, and doping is generally controlled by the fractions of Ag, Pb or Sb. The maximum ZT for LAST-m compound is about 1.7 at 700 K. The material shows p-type properties and an unusually low lattice thermal conductivity since the material forms spontaneously nanostructures during cooling from the melt, shown in Figure 2.3. However, the thermoelectric properties of the material are very sensitive to the synthesis conditions due to the complexity of the materials phase diagram. The formation of the nanoinclusions is believed to be caused by thermodynamic spinoidal decomposition or nucleation and growth events during cooling. The composition, structure, size and distribution of the nanoinclusions can be controlled by selection of the cooling rate and post synthesis heat treatment. [11]

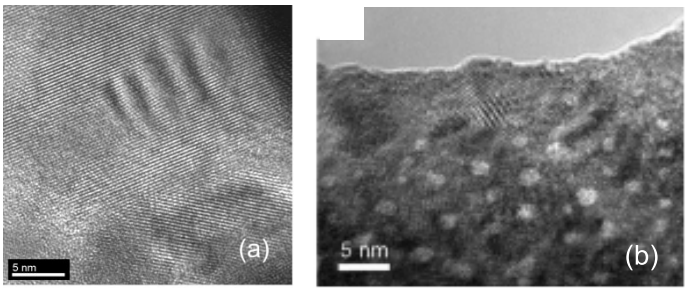

Figure 2.3: Transmission electron microscope pictures of (a) LAST and (b) SALT samples [11, 17].

$AgPb_mSn_nSbTe_{2+m+n}$, also known as LASTT, is similar material to LAST-m family with p-type characteristics and maximum ZT of about 1.4 at 700 K. The transport behaviour can be modified by tuning the Pb/Sn ratio instead of Ag or Sb concentrations as with LAST-m. $NaPb_mSbTe_{2+m}$, also known as SALT-m (sodium antimony lead telluride), is another high performance p-type material with ZT of about 1.6 at 675 K. As well as with LAST-m and LASTT, has SALT$-m$ nanosized inclusions of Na-Sb-rich cluster in the lattice , shown in Figure 2.3. SALT-m has one of the widest temperature ranges in which it has a ZT over 1, it reaches 1 at 475 K.

Silicon and germanium have both high carrier mobilities and lattice thermal conductivities. However, alloy of them is of interest for thermoelectric applications since lattice thermal conductivity of SiGe is about 15 % that of Si with only a little reduction in carrier mobility. Alloy scattering is also causing that majority of the heat is carried by low-frequency phonons. These are susceptible to boundary scattering, making it beneficial to reduce the grain size. Although this might reduce mean free path of electrons, some improvement has been reported. This is explained to be due to diamond crystal structure of SiGe. Due to the relatively high melting points and band gaps, SiGe is used in a high temperature regime (over 1000 K). However, the maximum ZT of the alloy remains between 0.5 and 1. It may be doped for p-type or n-type material. [4, 12]

Skutterudites such as $CoSb_3$ have an MX_3 composition and a crystal structure in which M atoms form a cubic framework surrounded by square arrangements of four X atoms. There is eight square arrangements for every eight cubes as illustrated in Figure 2.4. In such a structure there are voids that can be occupied by large metal atoms to form filled skutterudites. These loosely bound atoms are known as rattlers which can reduce the lattice thermal conductivity to an extremely low level. These guest atoms act as dopants as well, allowing p- and n-type doping. The smaller and heavier the ion is in the void, larger is the lattice thermal conductivity reductions due to larger lattice disorder [11]. Large power factor and low lattice thermal conductivity materials are sometimes referred to as phonon-glass electron-crystals (PGEC). Most often this concept is related to material development of skutterudites and clathrates, although it encapsulates the focus of research in the whole thermoelectric community. [4]

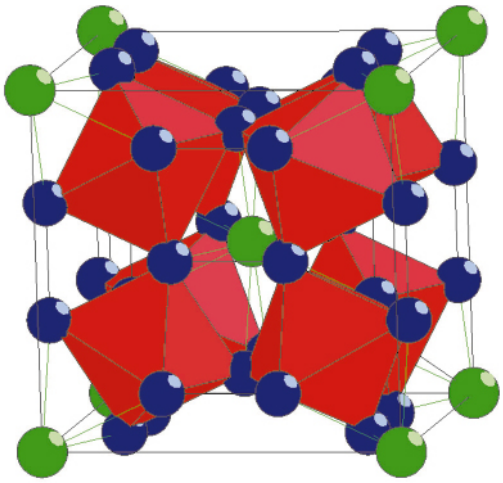

Figure 2.4: Crystal structure of filled skutterudites. M atoms are at the centre of the red octahedra and X atoms are the blue spheres. Voids in the lattice, that may be filled, are represented by green spheres. [11, 16]

ZT of skutterudites lies under unity in the temperature range of 500 - 700 K, but values approaching 1.4 at 1000 K have been predicted, making them highly promising compounds. The mechanism with which the rattlers reduce the lattice thermal conductivity is currently a subject of debate. Hypothesis based on the rattling induced phonon scattering has not been proven since it cannot be decoupled from scattering caused other factors, such as by point defects and lattice disorder. [11]

A novel class of thermoelectric materials are metal oxides. They are chemically inert in air and have high thermal stability making them interesting for high temperature applications. However, constructing modules can be difficult due to high contact resistances at metal/oxide interfaces and their differences in thermal expansion might cause cracking or exfoliation during operation cycles. Most promising oxide material is $NaCo_2O_4$, it has a layered crystal structure of CoO_2 sheets being confined by Na^+ ions that randomly occupy half of the interlayer atomic sites, illustrated in Figure

2.2. The CoO_2 sheets function as electron transport layers and Na^+ ions as phonon scattering region. ZT values of little over unity have been reported for $NaCo_2O_4$ at 800 K. [11]

In addition, oxides with interesting n-type properties are $SrTiO_3$ and ZnO. ZT of about 0.3 has been achieved at 1000 K by doping $SrTiO_3$ heavily with Nb and La as well as with Al-doped ZnO [11]. The drawback of $SrTiO_3$ is its considerably high lattice thermal conductivity, but there are good prospects of reducing it since the material has high effective mass and low mobility [4].

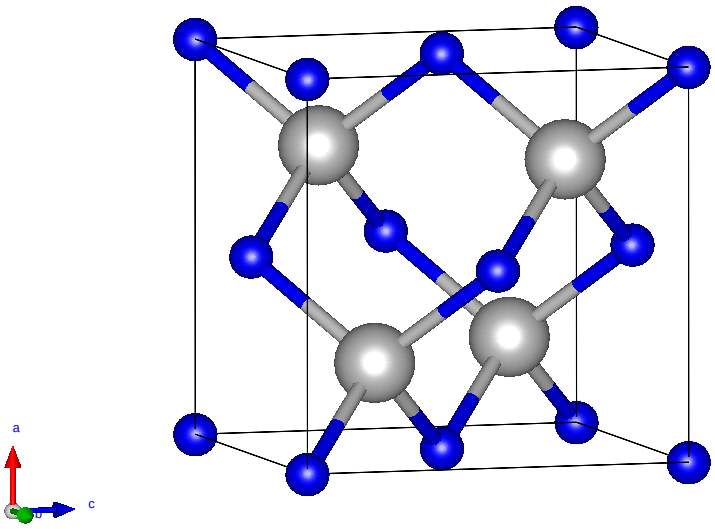

Figure 2.5: Zinc blende unit cell

ZnO, as most of the group II-IV binary semiconductors has either cubic zinc-blende (Figure 2.5) or hexagonal wurtzite structure (Figure 2.6). In wurtzite structure every Zn atom is surrounded by four O atoms which are coordinated at the edges of a tetrahedron. In the zinc-blende structure O atom is surrounded by 4 Zn atoms in similar fashion. These tetrahedral coordinations are typical for sp^3 covalent bonding, although ZnO has substantial ionic character as well; its ionicity resides at the borderline between covalent and ionic semiconductor. At ambient conditions it has wurtzite structure, whereas zinc-blende structure may be stable only when grown on cubic substrate. At relatively high pressures it may take cubic rocksalt structure as well since ionicity is favourable as lattice dimensions reduce. [18]

ZnO has a direct bang gap of about 3.3 eV at room temperature [18]. Hence, it is a high temperature thermoelectric material, with highest reported of ZT about

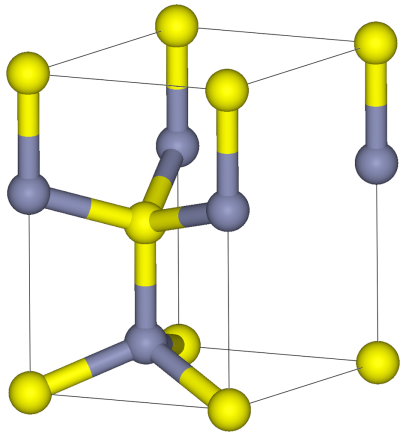

Figure 2.6: Wurtzite unit cell

0.65 at 1247 K with Al, Ga douping [19]. This is shown if Figure 2.7. ZnO has a high power factor (about 8 - 15 μW/cm K^2 from room temperature to 1000 K), but also high thermal conductivity (40 - 5 W/mK from room temperature to 1000 K) [11]. The decreasing thermal conductivity with increasing temperature is due to the Umklapp-process (explained in section 3.1) whereas thermally excited charge carriers reduce resistivity. Lattice thermal conductivity comprises about 90 % of the total thermal conductivity [20]. ZnO is intrinsically a n-type semiconductor. Aluminium is the most common n-type dopant for ZnO, but also In, Ga, Ti, Mo, Nb, Cu, Ge and Ca has been studied [11, 20, 21]. P-type doping with elements such as Li, Na, K, Ag, N ,P and As is also possible [18]. As nanostructuring has been utilized previously in the reduction of lattice thermal conductivity, thermoelectric properties of ZnO might be improved by those means.

As a summary, most of the high ZT materials have a form of complexity in their crystal structure and the fact that record ZT has been achieved by adding complexity further to such materials indicates that the key to high ZT material is complexity at multiple level and size scale.

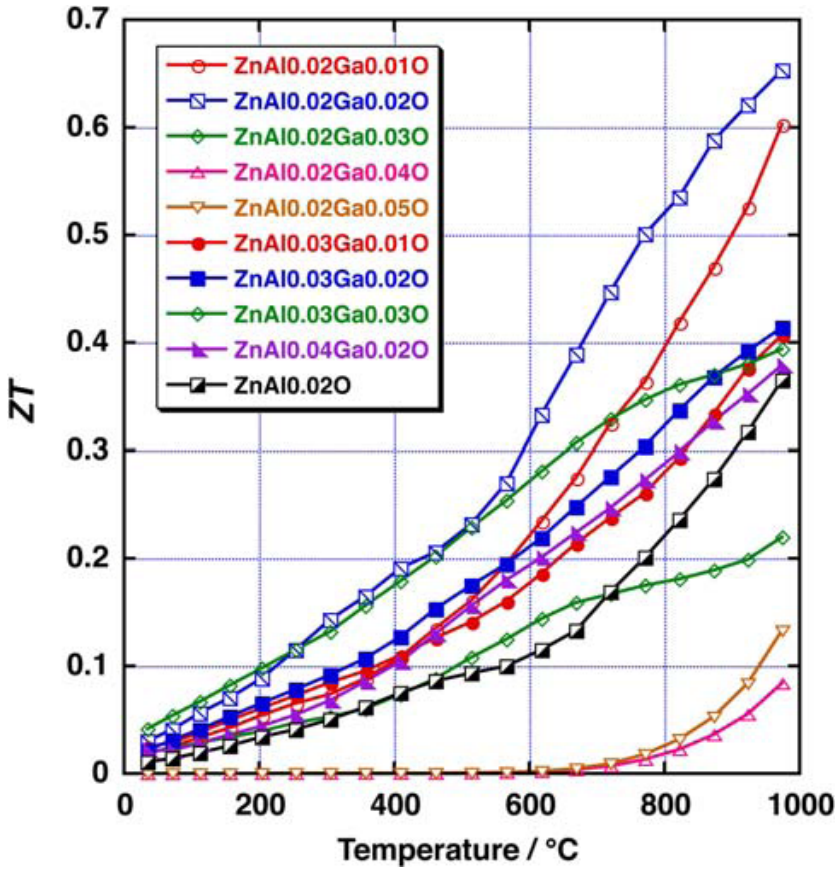

Figure 2.7: Temperature dependence of the dimensionless figure-of merit of $Zn_{1-x-y}Al_xGa_yO$ [19].

3 Thermoelectric conversion efficiency

3.1 Thermal conductivity

In a solid heat is conducted by lattice vibrations, phonons, and charge carriers. As atoms in a solid are bonded to their neighbours, any disturbance in an atom is passed on to the next one. Thus, atoms are in a permanent state of vibration and the overall motion can be understood as waves. The waves may be either longitudinal or transverse. Low frequency lattice vibrations are acoustic, but more important for heat conduction are high frequency optical waves. [4] The acoustic branch has a larger energy dispersion and thus greater distribution of phonon velocities, whereas optical phonons have quite weak energy dispersion. Since phonon group velocity is $v = \mathrm{d}\omega/\mathrm{dk}$, have optical branch phonons low v. This implies that they do not contribute to κ_l as $\kappa_l = Cvl$, where C is lattice heat capacity and l is phonon mean free path. [22]

If there are n atoms per unit cell, there will be three acoustic branches and $3(n-1)$ optical branches. Thus, materials with complex crystal structures, large n, have greater number of optical branches and reduced κ_l. This is presented with complexity factor, CF defined as the number of atoms per primitive unit cell. κ_l has been shown to be proportional to $CF^{-2/3}$. [22]

Phonons can interact with each other by normal (N) or Umklapp (U) processes, illustrated in Figure 3.1. They describe collisions of phonons in which N-process phonon momentum is conserved, whereas in U-process it is not. Thus, N-processes are important in distributing momentum, while U-processes lead to thermal resistance, net phonon backscattering and finite κ_l. U-processes can occur only when there are enough phonons with sufficiently large wave vectors to produce a resultant outside one unit cell, i.e. Brillouin zone. Thus, N-process scattering occurs within one unit cell only and state of the phonon changes, whereas in an U-process the phonon may scatter between unit cells. In order for the U-process to happen, the wave number must be greater or equal than minimum distance between of two adjacent unit cell boundaries, i.e. Fermi surfaces. Hence, in low temperatures where only long wavelengths, i.e. low wave number phonons are excited, U-process becomes less likely. At high temperatures U-processes become more and more probable as high wave number phonons are excited. Worth noting is that the word Umklapp means turning over, which comes from the mathematical interpretation of the phenomenon. The processes are represented in terms of the wave vectors q as

$$q_3 = q_1 + q_2, (\text{N-process}) \tag{3.1}$$

and

$$q_3 = q_2 + q_1 + \text{G}.(\text{U-process}) \tag{3.2}$$

The scattered phonon is turned back into the same Brillouin zone where it came from by addition of a lattice wave number, i.e. the reciprocal lattice vector G. This can be done since both Brillouin zones are equivalent representations of the same states. [4, 22, 23]

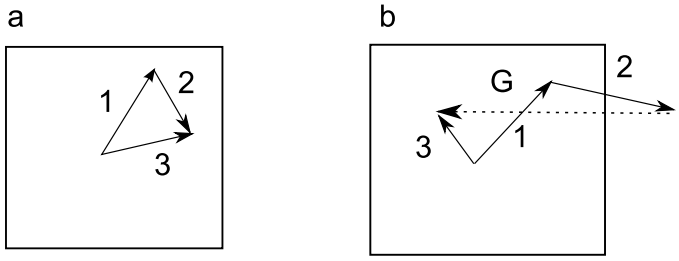

Figure 3.1: Representation of a) N-process and b) U-process

Phonon mean free path can be considered via relation to the phonon wavelength. Phonon wavelength, λ_{ph}, may vary from the spacing between two lattice points up to the sample size. At the minimum value of λ_{ph}, minimum value of κ_l is also reached for certain C and v. Introduction of minimal value for lattice thermal conductivity emphasizes the need to pay attention to the enhancement of the power factor as κ_l cannot be indefinitely reduced. However, in the presence of nanostructures of comparable size to l, the temperature gradient across the nanostructure might not be well defined. This indicates that Fourier heat conduction would no longer apply, but instead the heat transport should be considered as radiative. As a result κ_l would be reduced by increasing the ratio of l to the sample size. [22]

When the flow of phonons and charge carriers becomes linked, phonon drag effects appear. Momentum of the phonons is being transferred to the charge carriers. Generally, the phenomenon becomes significant at low temperatures (≤ 20 K), where voltages of 5 - 20 mV/K have been obtained due to the phonon drag [22]. However, the phenomenon becomes smaller as charge carrier concentration increases. This is due to the increase of the momentum being transferred back to the electrons from the phonons. This is thought to prevent the use of phonon drag as a mean of improving ZT. [4] Nevertheless, in Si nanowires an increased thermopower, 350 $\mu V/K$ at 200 K, due to phonon drag has been observed. It is claimed to be due to three-dimensional to one-dimensional crossover of the phonons participating in phonon drag [24]. The crossover should remove the cross-sectional wire dimensions from limiting phonon mean free path.

Phonons in a lattice are scattered not only by other phonons but also by various types of defects and boundaries. For solid solutions between two semiconductors of same crystal structure, such as SiGe, the scattering is based on local changes of density, or elastic constants related to different atoms that cause local changes in the speed of sound [4]. Rayleigh theory can be applied, albeit for higher frequency phonons the defect size is of same size as is the wavelength of phonons. Generally the concept is applicable only when the defect is much smaller than the wavelength

of the phonons. Nonetheless, high frequency phonons are strongly scattered having little contribution to κ_l. Hence, the scattering cross-section, i.e. likelihood of a phonon being scattered by a particle is given by

$$\sigma_s = \frac{4\pi {d_{pd}}^6 q_L^4}{9} \left(\frac{\Delta\chi}{\chi} + \frac{\Delta\rho_d}{\rho_d} \right)^2, \tag{3.3}$$

where d_{pd} is the diameter of the defect, q_L is the magnitude of the phonon wave vector, χ is the local change of compressibility, and ρ is the local change of density. Majority of the scattering is believed to be caused by mass-fluctuations. Fluctuations in elasticity are caused by foreign atoms whose bonds differ from that of host atom and who do not fit well into the lattice site, straining the crystal. Both elasticity and mass-fluctuations cause local changes in the speed of sound. [4]

Crystal boundaries are able to scatter phonons in semiconductors. Even though phonons have usually wavelengths of a few nanometres at ordinary temperatures are micrometer size grains efficient in reducing the lattice thermal conductivity. Phonon mean free path varies strongly with their frequency. Low frequency phonons have sizeable contribution to κ_l since they have large mean free path, despite being few in number. Assuming that relaxation time for Umklapp scattering is proportional to ω^{-2}, all frequency componenets make comparable contribution κ_l since according to the Debye theory the number of phonons at angular frequency ω is proportional to ω^2. This illustrated by the upper curve in Fig. 3.2. Point defect scattering will remove the contribution of the most high-frequency phonons according to 3.3 since q_L is directly proportional to the frequency. The remaining low frequency phonons are sensitive to boundary scattering due to their long free path. [4]

The lattice thermal conductivity of a large pure crystal is represented by area under the upper curve in Fig. 3.2. The lattice thermal conductivity can be estimated by the ratio of the unshaded area to the total area. There are regions where more than one of the scattering mechanisms are present leading to more gradual cut-offs, but the error is not great since variation of relaxation time with frequency is quite different for Umklapp, point-defect and boundary scattering. [4]

Most thermoelectric materials have several atoms in their unit cell, having more optical modes than acoustic modes in their fibrational spectrum. However, most heat should be carried by low-frequency acoustic modes since the group velocity of optical modes is relatively low. Nonetheless, due to their large number, they might have significant contribution, but its magnitude is difficult to estimate. As a result, boundary scattering in material with large unit cell is well to described with the difference between the lattice conductivities in the material with large and small crystal size. [4]

As Umklapp scattering takes over from boundary scattering at the frequency of $\omega_0 = \sqrt{\frac{V}{BL}}$, the contribution to κ_l from phonons with frequencies below this limit is to be determined. The specific heat of the low-frequency modes with and without

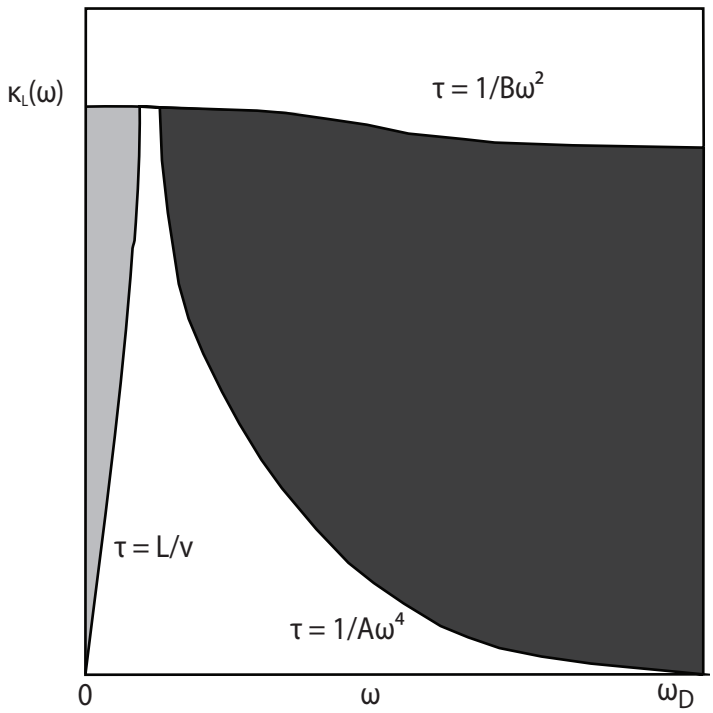

Figure 3.2: Contribution of phonons at angular frequency ω to lattice thermal conductivity. The upper curve illustrates Umklapp scattering, the right curve point defect scattering and the left one boundary scattering. Thus, the black area presents contribution removed by point defect scattering and gray contribution removed by boundary scattering. L is the width of the crystal and V is the velocity of sound. A and B are material parameter constants.

boundary scattering can be determined using the Debye model. As a result, κ_l is reduced by two thirds. This reduction is determined to become noticeable when the grain size falls below 10 μm. [4]

Thermal conduction across a boundary/interface can be explained with the acoustic mismatch (AMM) theory and diffuse mismatch theory (DMM). In the AMM, both sides of the interface are treated as a continuum, each with an acoustic impedance $A = \rho_d V$, where ρ_d is the density of the material and V is the speed of sound in the material. The interface is treated as a plane. The continuum approximation should be accurate to phonons with wavelength much greater than theinteratomic spacings. Thus, when a phonon is incident on a interface it can only specularly reflect, reflect and mode convert, refract, or refract and mode convert. The angles for these can be determined applying Snell's law. Thus, the angle of transmission from medium 1 to 2 is

$$\sin\theta_{tran} = \frac{v_p^2}{v_p^1}\sin\theta_{in}, \tag{3.4}$$

where v_p is the phonon velocity and θ_{in} is the angle of incidence. As the transmitted angle cannot exceed 90°, angles for which sin θ_{in} is greater than v_p^1/v_p^2 cannot be transmitted. These are called critical angles. On the side with the greater phonon velocities, there are no critical angles and phonons with any incident angle may be transmitted. The probability for transmission [22] is determined by Fresnel equations and transmission from medium 1 to 2 is

$$T = \frac{4(A_2/A1)(\cos\theta_{tran}/\cos\theta_{in})}{((A_2/A_1) + (\cos\theta_{tran}/\cos\theta_{in}))^2}. \tag{3.5}$$

The heat flux across the interface is determined by the product of the incident number of phonons and T. Thus, the maximal heat transfer occurs when the two materials have similar values for the mass density and specific heat. However, the model ignores the possibility of scattering at the interface as well as transmission probability being independent of phonon frequency. [25]

The diffuse mismatch theory assumes that all phonons are diffusely scattered at an interface. Thus, probability of transmission is determined by the mismatch between phonon density of states into which the phonon can scatter. This is caused as correlations between incoming and outgoing phonon wave vectors are assumed to be destroyed by diffuse scattering. Hence, the probability of phonon scattering into one side of the interface is independent of where it came from. Thus, all correlations between incoming and outgoing phonons are ignored except energy. Also, structure of the scatterers is ignored. Transmission probability with such conditions is

$$T_i(\omega) = \frac{\sum_j c_{3-i,j} N_{3-i,j}(\omega, T)}{\sum_{i,j} c_{i,j} N_{i,j}(\omega, T)}, \tag{3.6}$$

where $N_{i,j}$ is the phonon density of states on the side i and mode j (longitudinal or transverse) and c_i is the speed of sound. Notation 3-i denotes side opposite to i. In comparison to AMM the result obtained with DMM is the same as if the difference in acoustic properties is small, as with most solid-solid interfaces. In such a case roughly half of the phonons are transmitted for both models since the mismatch in the density of phonon modes is small as well. However, if the acoustic mismatch is large, DMM predicts larger value for transmission probability than AMM. Moreover, in the case of a boundary with identical acoustic properties, AMM predicts a transmission probability of 100 %, whereas DMM predicts a probability of 50 %. [25]

When phonons are considered as waves, which must be done when $d < l$ (d is the spacing between films/interfaces and l is phonon mean free path), the propagation is covered by a form of Bragg's law $n\lambda = 2d\cos\theta_k$, where θ_k is the angle between phonon propagation and plane of the interface, or superlattice growth direction. For instance, when a phonon travels perpendicular to an atomically perfect interface,

complete backscattering due to constructive interface occurs if $\lambda_{phonon} = 2d$. The interface roughness should be less than phonon coherence length of 1 nm in order to be clearly manifested. The selective backscattering or transmitting of phonons gives the rise for phonon filter and phononic band gaps. [22]

A way to modulate thermal conductivity in a structure is by introduction of a binary multilayer system ($d = d_1 + d_2$) in which different phonon propagation velocities may interference inducing a phononic band gap whose magnitude is dependent from the difference in acoustic impedance of the layers. As such a system allows only certain phonon frequencies to be transmitted, can lattice thermal conductivity be reduced by flattening of the phonon dispersion. This results in reduced phonon group velocity. The regulation can be achieved through changing the layer thickness or by the choice of materials. The layer thickness affects the frequency of transmission and the material pair determines the acoustic impedance. [22]

The way to realize a phononic band gap is to have a periodic array of inclusions embedded in a matrix. In order to achieve a wide band gap, large acoustic contrast between the matrix and the inclusions is required as well as sufficient filling factor of the inclusions. Geometry of the inclusions is important as well. [26] Forbidden frequency gap is formed as certain transverse (T) modes at high phonon frequencies are folded back into the main Brillion zone from vicinity of the Brillion zone edge. As a result, a crossing type interaction with longitudal (L) mode is avoided. In other words, the band gap is formed by inter-mode Bragg reflection with a wave vector conservation $k^L + k^T = 2n\pi/d$ for the normal component, and $k^L = k^T$ for the parallel component. The formation of band gaps enables L - T mode conversion, leading to that at an interface the transmitted and reflected waves could carry equivalent amounts of energy, yielding no net energy transport. [22]

3.2 Nanostructuring in reduction of thermal conductivity

In order to characterize phonon population, parameters such as median wavelength for thermal conductivity λ_{50} is needed. The parameter is defined such that 50 % of the heat is carried by wavelengths shorter than λ_{50}, and 50 % is carrier by wavelengths longer than λ_{50}. In order to describe the width of the phonon distribution, wavelength cutoffs of 10 % (λ_{10}) and 90 % (λ_{90}) for the heat transport are also introduced. As nanostructures are dominated by boundary scattering, the frequency dependency of the mean-free path is neglected. Thus, the phonon distribution weighted by thermal conductivity is defined by

$$\int_{\lambda_{min}}^{\lambda_\alpha(T)} C_\lambda(\lambda, T) v(\lambda) d\lambda = \alpha \int_{\lambda_{min}}^{\lambda_{max}} C_\lambda(\lambda, T) v(\lambda) d\lambda, \tag{3.7}$$

where C_λ is the spectral specific heat per unit wavelength, v the spectral group velocity and $\lambda_\alpha(T)$ is the wavelength below which the fraction of α of the heat is carried. For example, for material with v_s of 5000 m/s at 10 K with mean free

paths limited by boundary scattering, 90 % of the heat is carried by phonons of wavelength less than about 11.3 nm. However, analogous equation calculated for phonon number shows that 50 % of the phonons have wavelength less than about 10.2 nm. Thus, about 90 % of the heat is carried by 50 % of the phonons. [3]

Most thermoelectric materials are used at relatively high temperatures and much higher temperatures than in previous example. Above cryogenic temperatures, is λ_{90} of about 2 nm and λ_{50} is about 1 nm. Therefore, only in the very thinnest nanostructures are the structure sizes comparable to the important wavelengths. This implies that for transport parallel to interfaces the phonon dispersion remains unchanged compared to bulk material. However, for transport perpendicular to interfaces the average group velocity can be reduced regardless of the structure size. [3]

The small typical wavelength gives rise to diffuse scattering to take over from specular scattering at normal temperatures. Perfectly diffusive scattering, scatters phonons randomly leading to large thermal resistance both parallel and perpendicular to interfaces. The specularity depends on the ratio of surface roughness to wavelength. When wavelength is five to ten time smaller than surface roughness full specularity is achieved. As nanowires and superlattices typically exhibit 1 or 2 nm of roughness, diffuse scattering is expected. Reducing thermal conductivity in this manner is possible as electron scattering at an interface is determined by the differences in electrostatic potential. Furthermore, electron wavelengths in normal temperatures tend to be much longer than those of phonons. Thus, a surface that scatters phonons diffusely may scatter electrons specularly. [3]

Similar to equation 3.7, cutoff mean-free paths, L_α, which account for a fraction of α of the total heat flux, can be calculated in order to understand the range of important mean-free paths for lattice thermal conductivity. The calculation shows that 50 % of the heat in bulk Si at 300 K is carried by phonons of mean-free path up to 580 nm and only 10 % of the heat is carried by phonons with mean-free path less than 87 nm. In order to account 90 % of the heat flux, mean-free paths up to 12.8 μm must be considered. Practical thermoelectric materials, such as PbTe, have already low thermal conductivity compared to Si. However, the low thermal conductivity is due to lower group velocity. The mean-free paths of PbTe at 300 K are about an order of magnitude lower than that of Si, nevertheless 80 % of the heat is carried by phonons with mean-free paths between 6 nm and 860 nm. The cutoff mean-free paths of Si and PbTe are illustrated in Figure 3.3. Thus, nanostructuring seems an effective means to reduce the thermal conductivity via reducing the phonon mean-free path.

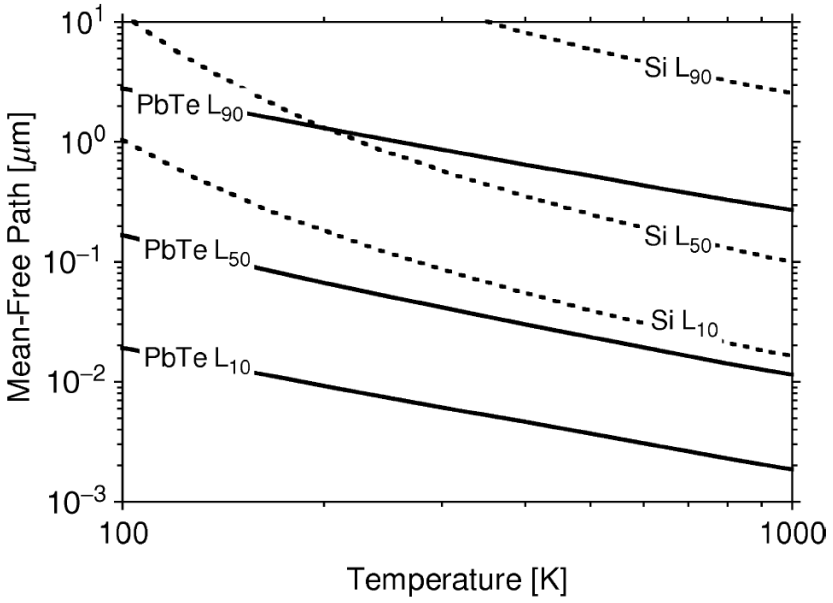

Figure 3.3: Important mean free paths for carrying heat in bulk Si and PbTe. [3]

3.3 Nanostructuring for enhancement of power factor

Increasing the Seebeck coefficient of a material without decreasing the electrical conductivity is a major goal of the thermoelectric research. Nevertheless, it is not well understood which materials will have high power factor. As explained in section 1, generally electrical conductivity and Seebeck coefficient change in opposite directions with charge carrier concentration.

The number of valence (p-type) or conduction (n-type) band extrema is an indication for higher S. The extrema are populated by charge carriers forming carrier pockets [11]. The six carrier pockets of Bi_2Te_3 are shown in Figure 2.1. The valleys may be thought to be distinct each having distinct transport coefficients, thus the transport coefficients for a material may be summed from those of the band. Moreover, in case of mixed charge carriers is Seebeck coefficient cancelled. [22]

The maximum attainable figure of merit derived from Boltzmann equations is

$$Z_{max} \propto \gamma \frac{T^{3/2\tau_z}\sqrt{\frac{m_x m_y}{m_z}}}{\kappa_{ph}} e^{(r+1/2)}, \tag{3.8}$$

where γ is the degeneracy of band extrema, m_i is the effective mass of charge carriers in i-th direction, t_z is the relaxation time of charge carriers in transport direction z, r is the scattering parameter and k_{ph} is the lattice thermal conductivity. The equation implies that if the transport is along the z-direction, a small effective mass

coupled with very large masses along x and y directions should lead to a high ZT. Such a system is expected to have high anisotropy in the electronic as well as in crystal structure. [11]

Although, both equations 3.8 and 3.9 are exactly valid only for homogenous single phase compounds, they are assumed to be valid for nanocomposites as well [11].

The size of the band gap determines the temperature limit, where the doped semiconductor becomes intrinsic due to the thermal activation of minority charge carriers. High band gap leads to high temperature limit. [11]

The way in which the details of electronic structure affect the Seebeck coefficient are partly explained by Motts equation

$$S = \frac{\pi^2 k_B^2 T}{3e} \frac{d \ln(\sigma(E))}{dE}_{E=E_F}, \tag{3.9}$$

where $\sigma(E)$ is the electronic conductivity as a function of the Fermi energy E_F. As $\sigma(E) = g(E)e\mu(E)$ and $n(E) = g(E)f(E)$ we get

$$S = \frac{\pi^2 k_B^2 T}{3e} \left\{ \frac{1}{\mu} \frac{d\mu(E)}{dE} + \frac{1}{g(E)f(E)} \frac{dg(E)f(E)}{dE} \right\}_{E=E_F}, \tag{3.10}$$

where $g(E)$ is the electronic density of states (DOS), $\mu(E)$ is the charge carrier mobility, $n(e)$ is the charge carrier concentration and $f(E)$ is the Fermi function [27].

Thus, a material with rapidly changing DOS near E_f is expected to have larger S than one with flatter DOS near E_f. In other words Seebeck coefficient is a measure of asymmetry in the electronic structure and scattering rates near the Fermi level. Such asymmetry may be induced by disturbances in electronic structure and scattering rates within a small energy interval near E_F. [11] Seebeck coefficient may be increased by increasing energy dependence of $\mu(e)$ or $n(E)$. The charge carrier mobility might be increased by a scattering mechanism that strongly depends on the energy of charge carriers. The energy dependence of charge carrier concentration may be increased by a local increase in DOS. This is the basis of Mahan-Sofo theory [28]. The theory suggests that a local increase in DOS over a narrow energy range will enhance the Seebeck coefficient. Moreover, theory states that a delta-shaped transport function should maximize ZT suggesting that a narrow distribution of energy carriers with high velocity in the direction of the applied field is the wanted property. However, the study concludes that with an addition of more than 1% constant background transport distribution to the integrated contribution of the peak will not lead to increased figure of merit.

Enhancement of the thermopower by tuning DOS has been demonstrated [27] via impurity-induced band distortion. The band distortion was believed to be caused by Tl induced additional energy states, resonant levels. The levels are speculated to rise due to valence fluctuations or by hybridization between an excited state

and neighbouring Te p-state. The band distortion was shown by Nernst coefficient measurements. By comparing the Seebeck coefficient to the hole concentration, it was discovered that S was enhanced for certain charge carrier concentrations by more than a factor of 2. Moreover, effective mass was found to increase by a factor of 3 compared to Na^+ doped counterpart. However, in comparison with traditional PbTe ZT is not significantly improved. Na doped PbTe has similar ZT as is reported in [29].

Electrical density of states is the number of states per energy range that are available to be occupied by electrons, i.e. number of states whose allowed wave vector falls within the energy range. When the motion of an electron is limited to lower dimensions, will the modification of the energy spectrum lead to an enhancement of the density of states. The density of states (DOS) per unit volume for a single band/subband in three-, two- and one-dimensional systems, including a spin-degeneracy factor of two are

$$g_{3d}(E) = \frac{1}{2\pi^2}\left(\frac{2m_d}{\hbar^2}\right)^{3/2} E^{1/2}, \quad E \geq 0\,, m_d = \sqrt[3]{m_x m_y m_z} \tag{3.11}$$

$$g_{2d,n}(E) = \frac{m_d}{a\pi\hbar^2}, \quad E \geq E_n\,, m_d = \sqrt{m_x m_y} \tag{3.12}$$

$$g_{1d,nm}(E) = \frac{1}{a^2\pi}\left(\frac{2m_d}{\hbar^2}\right)^{1/2} (E - E_{nm})^{-1/2}, \quad E \geq E_{n,m}\,, m_d = m_x \tag{3.13}$$

where a is the physical length scale, $\hbar$ is the reduced Plank constant, m_x, y, z are the principal effective masses in x-, y-, and z directions and E_n is the confinement energy. [22]

As can be seen from Figure 3.4, the total DOS is the superposition of all the subbands. The strategies for utilization of the phenomenon in enhancement of the power factor lie in the change of the energy dependence of DOS with dimensionality and the inverse proportionality of DOS to the dimension.

Electrical conductivity is given by

$$\sigma = \frac{e^2}{3\hbar}\int dE v^2(E) g(E)\tau(E)\left\{-\frac{\partial f(E)}{\partial E},\right\} \tag{3.14}$$

where τ is the electron relaxation time and v is the Fermi velocity. The equation shows that the shape of $g(E)$ plays no role in determination of electrical conductivity. Furthermore, the enhancement of Seebeck coefficient via narrowing the density of states has been questioned in ref. [22] as the average energy is slightly larger in bulk

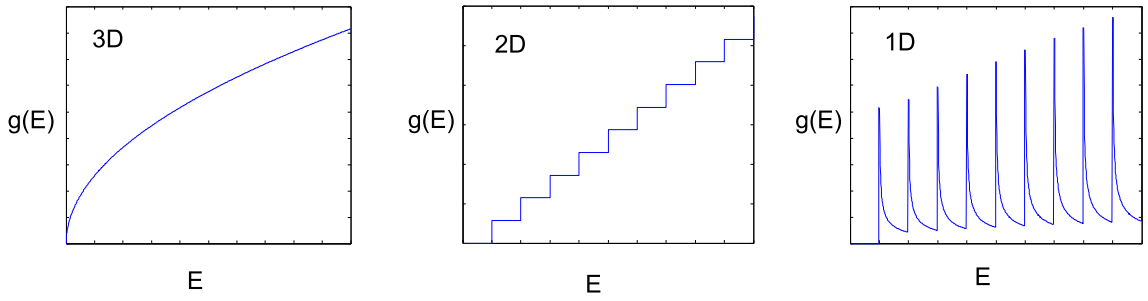

Figure 3.4: Schematic representation of density of states in 3D, 2D and 1D material.

material corresbonding to parabolic DOS than with step or peak like DOS if they both have the same Fermi level. The Bulk DOS favours high energy states while nanowire DOS is skewed toward lower energy states.

4 Thermoelectric measurements

Accurate measurement and characterization of electrical and thermal transport properties of thermoelectric materials possesses many challenges.

The Seebeck coefficient metrology lacks Seebeck coefficient standards and consensus of the time scale definition. Moreover, often publications contain poor estimations of uncertainty and minimal details in apparatus descriptions. Terminology is often inconsistent as well. [30]

4.1 Seebeck coefficient metrology

Spatial arrangement of probes may affect the results, even though the Seebeck coefficient is not geometry dependent. In the two-probe (or axial-flow) technique, temperature difference and the electronic potential are measured on the probes which are in contact with the ends of the specimen. Thermal and electrical contacts are optimal using the two-probe technique [30]. However, four-probe (potentiometric) technique is often preferred for the possibility of simultaneous resistivity measurement. In the four-probe technique the temperature and the voltage are measured at two points on the sample equidistant from the hot and cold sinks on the axis parallel to the heat flow. In order for this method to be accurate, the diameter of each probe must be much smaller than the effective distance between them. Four-probe method is considered to be beneficial for longer and narrower samples, whereas two-probe method may benefit shorter or disk-shaped samples as far as the thermal resistance of the sample is larger than thermal contact resistance. [30]

Reliable Seebeck coefficient measurement requires spatially and temporally synchronous measurement of voltage and temperature; the probes being in very good thermal and electrical contact with the specimen; and acquisition of microvoltages without external constituents. As the temperature difference is most often done by thermocouples, both the temperature and voltage measurements are essentially low voltage measurements. [30]

Integral (large ΔT) and differential (small ΔT) methods are employed to measure the relative Seebeck coefficient. In the integral method, one end of the sample is fixed at certain temperature, while the opposite end is heated. The data acquired is then fitted to an appropriate analytic approximation. The method succeeds in minimizing the influence of the voltage offset and is most useful for longer samples that show metallic behaviour. However, maintaining one end of the sample at constant temperature is difficult as is obtaining a satisfactory fitting. Moreover, there are no objective criteria to evaluate the accuracy of the obtained result. [30]

Most of the Seebeck coefficient characterizations are done with the differential method. A small thermal gradient is applied across the sample, which is being held at mean temperature of the cold and the hot end. This method yields the Seebeck coefficient exclusively by the ratio of electric potential and the temperature difference as long as the temperature difference is much smaller than the mean

temperature and contact potential much smaller than the voltage generated by the Seebeck effect. [30, 31]

The following sections describe the different realizations of the differential methods. They are categorized according to the observation time scale, i.e. the interval required for one voltage measurement. [30]

4.1.1 The steady-state method

Under steady state conditions the Seebeck coefficient is often calculated from the linear fit of multiple electric potential/temperature data points. Thus, it is avoided that the curves intersect at the origin i.e. $V_{AB} = 0$ and $\Delta T = 0$. For this reason, the offset voltages arising from the thermocouple inhomogenities and non-equilibrium contact interfaces are eliminated. The selected temperature differences must increase slowly in order to satisfy the assumption of linearity. [30]

4.1.2 The quasi-steady-state method

The quasi-steady-state method measures simultaneously multiple electric potential/temperature difference data points by continuously increasing the heat flux. Such a measurement reduces the contribution of offset voltages as well as reduces the time needed to properly stabilize each ΔT. However, the method relies on voltage measurements with uncertainties in the order of nanovolts. Obviously, with the use of voltage channel switches in such a fast measurement would be unlikely to yield correct data. This is due to delays caused by the switch units as well as transient signals and thermal offsets arising from the relays. Moreover, there is no clear guidelines for proper selection of time rates for change in the temperature difference. [30]

4.1.3 The transient method

The transient method utilizes sinusoidal temperature difference $\Delta T \sin(\omega t)$ in order to circumvent the demand for stable temperature difference. Typically the temperature difference is under 0.5 K and the frequency below 60 Hz. Lock-in amplifiers are used to monitor corresponding voltages for the determination of the Seebeck coefficient. The method allows the use of smaller temperature differences than steady-state methods as well as eliminates extraneous voltages rapidly by modulating of temperature difference. Hence, structural resolution of Seebeck coefficient may be sharpened. However, the method is more sensitive to the thermal diffusivity, heat capacity, mass and geometry of the sample. Thus, measurements are sensitive to the position of the thermocouples, sample thickness and the input frequency. The frequency should be adjusted according to the thermal diffusivity or the sample length in order to ensure proper attenuation of ΔT to the cold end. The sample thickness should be significantly smaller than thermal diffusivity length, $\lambda = (D/\pi f)^{1/2}$),

where D is the thermal diffusivity of the material and f the frequency. Nevertheless, ΔT may have slight frequency dependence above about 1 Hz. Moreover, there are no objective criteria to choose the appropriate frequency. [30]

All measurements systems described in this chapter measure the value of a thermocouple, a sample and a reference wire. Thus, the value of the reference must be determined in a separate experiment. There are two methods for measuring the absolute Seebeck coefficient. In low temperature, a superconductor may be used as a reference material as their Seebeck coefficient is zero when they are superconductive. At higher temperatures S for pure materials can be calculated from Thomson heat μ_T with

$$S(T) = \int_0^T \frac{\mu_T}{T} dT. \tag{4.1}$$

Seebeck coefficient should be measured during both heating and cooling cycles to ensure repeatability and confirm that sample has not changed. Deviation should be within $\pm$ 5 $\mu V/K$ [32].

4.2 Resistivity

Often resistivity is measured with the same device as the Seebeck coefficient [30]. Resistivity of thin films or thin discs may be measured using the four-point [33] or van der Pauw [34] techniques. In the four-point method, four needle point probes are collinear and evenly spaced along the sample, current, I, is fed through the outer probes and corresponding voltage, V, measured via the inner probes. The resistivity of the four-point technique is given by

$$\rho = (\frac{(Vw)}{I})C_1(a/d)C_2(w/s), \tag{4.2}$$

where w is the thickness of the sample, s is the spacing between contact probes, a is the sample dimension parallel to contact line, d is the sample dimension perpendicular to contact line, $C_1(a/d)$ is a correction factor for planar dimensions and $C_2(w/s)$ a correction factor for the ratio of thickness to the contact spacing. This is illustrated in figure 4.1.

Van der Pauw method allows direct determination of resistivity. It requires that point contacts are placed on the extreme edges of the sample. The resistivity is given by

$$\rho = \frac{F}{2}\frac{\pi w}{ln2}(R_{AB,CD} + R_{BC,DA}), \tag{4.3}$$

where $R_{AB,CD}$ is V_{CD}/I_{AB}, $R_{BC,DA}$ is V_{AD}/I_{BC} and F is a function of the ratio $R_{AB,CD}/R_{BC,DA}$. If $R_{AB,CD}/R_{BC,DA} \leq 1.5$ is F ≈ 1. The error for the placement of

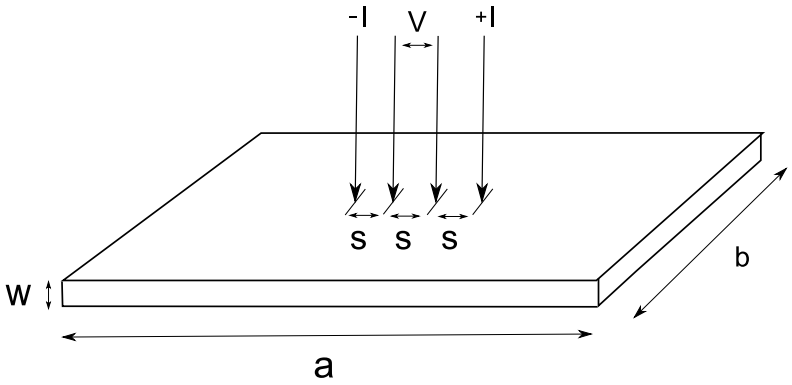

Figure 4.1: Schematic presentation of the four point measurement scheme.

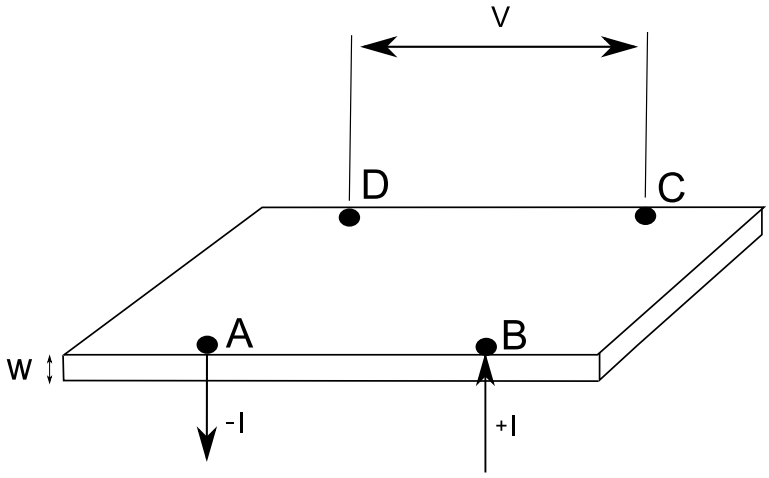

Figure 4.2: Schematic presentation of the Van der Pauw measurement scheme.

the contacts onto the sample is given by

$$\frac{\Delta\rho}{\rho} = -(ln\frac{1+(b/D)^2}{1-(d/D)^2})(\frac{1}{2ln2}), \tag{4.4}$$

where b is the distance from the edge to the point contact and D is diameter of the sample. This is illustrated in figure 4.2.

General requirements for the resistivity measurements include having a good electrical contact and accurate determination of sample dimensions. Moreover, as thermoelectric material has high Seebeck coefficient, measurement current may induce the Peltier effect leading to the Seebeck voltage being added onto the resistive voltage drop. The effect may be minimized by making the measurement relatively fast or by alternating current polarity and averaging the result. [3]

Fabrication of good electrical contact on metal-semiconductor interfaces may be

difficult. Oxide layers are often on the surface and p-n or Schottky-junctions can lead to erroneous resistivity measurements. [3]

4.3 Measurement device for determination of Seebeck coefficient and resistivity

A measurement device to characterize electrical resistivity and thermopower of semiconductor materials in the temperature range of 120 - 380 K was built. The resistivity measurement utilizes the van der Pauwd method and the thermopower measurement is done with the steady state method. The device consists of four needle probes contacting the sample at its circumference. A T-type thermocouple (i.e. constantan wire) is connected between Peltier element and ceramic support in order to measure their temperature difference. The Peltier element is used to create a temperature gradient across the sample and the ceramic support functions as a thermal well. One of the needles is fixed and the three remaining are movable allowing the measurement of samples with diameters between 7 - 30 mm. This is illustrated in Figure 4.3. The thermal insulations and mechanical fixings of the measurement device of the device are shown in Figure 4.4.

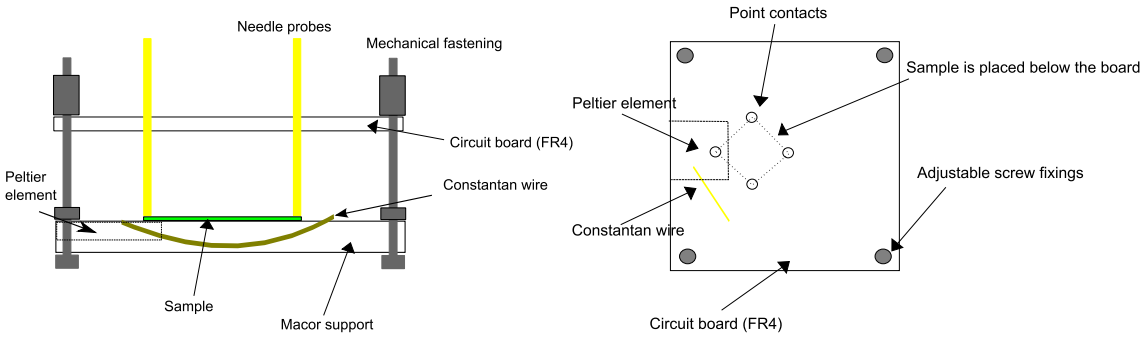

(a) Side view (b) Top view

Figure 4.3: Schematic presentation of the measurement setup.

The resistivity is measured with a multimeter (Agilent Technologies 3458A) with the four-point measurement scheme. A switch (Agilent Technologies 3488A) is used to change the test lead contacts to measure R_{AB} and R_{BC}. Average of three 1 second measurements is taken as a value for each R_{AB} and R_{BC}. The temperature of the support is measured with a K-type thermocouple and the voltage is measured with a multimeter (Fluke45).

The Seebeck coefficient is measured by heating one corner of the sample by a peltier element at constant power. Once steady temperature difference is reached the temperature difference is measured with copper-constantan thermocouple. The thermoelectric voltage generated by the sample - needle probes thermocouple is measured at the same time. This is done three times at three different heating powers i.e. temperature differences. A linear line is fitted to the obtained data point and slope

of the line is the Seebeck coefficient. Both voltages are measured with multimeters (Agilent Technologies 3458A and 34420A).

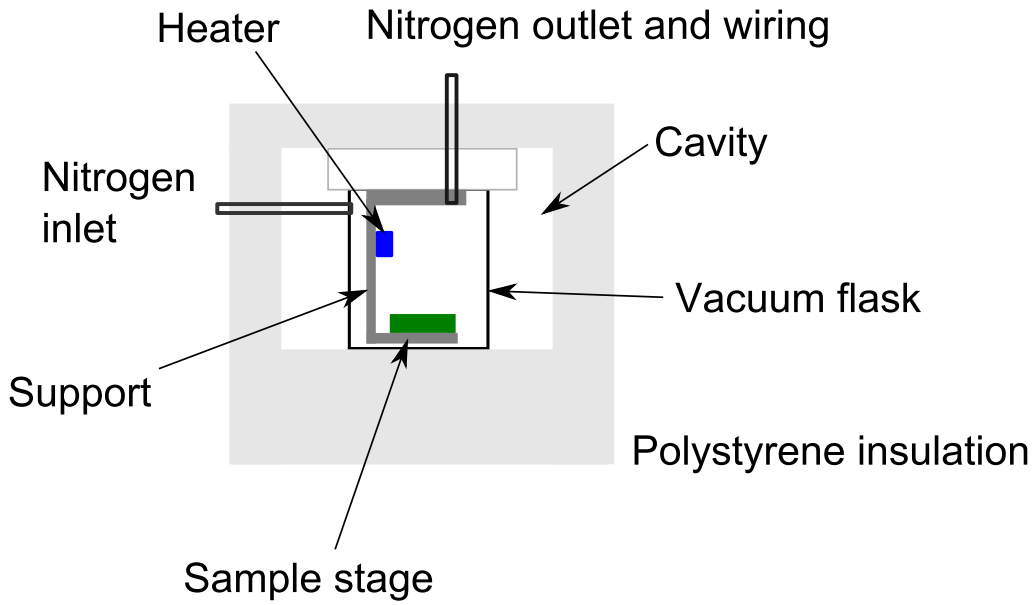

Figure 4.4: Schematic presentation of the thermal insulations and mechanical fixings of the measurement device. Low temperatures can be reached by flooding the cavity with liquid nitrogen and resistive heater is used to achieve temperatures above the ambient. Sheet flow of nitrogen is required to prevent the deposition of ice at low temperatures.

Measurement errors rise due to inaccuracies in multimeters, measurement scheme and measurement setup. The accuracy of the multimeters is presented as ± (ppm of Reading + ppm of Range) (Agilent) or ± (percentage of reading + digits) (Fluke). In the case of Agilent 3458A and 34420A this corresponds to an error of about ± 0.6 μV when measuring in the μV range. For resistivity measurement the error is about ± 6 mΩ. These are negligible compared to other errors. However, the Fluke 45 multimeter has an accuracy of about ± 6 μV, which causes an error in the Seebeck absolute temperature measurement. However, as the reference function is not stabilized, it remains the main source of error in the absolute temperature reading. The main cause of error for the resistivity measurement rises from the placement of the contacts given by equation 4.4. In addition, the uncertainty of ellipsometer measurement of the film thickness is about 3 %. For small samples this may easily add up to 15 %.

Main source of error in the Seebeck measurement lies in the measurement geometry. As the sample is heated from below it and the voltage is measured above it, a significant error is unavoidable. Although Peltier elements are ideal to create stable temperatures, heat losses due to the measurement probes, convection and radiation cause the temperature at the sample surface to be a bit lower than that of at the heater below the sample even for the thinnest of samples. In order to

have a estimation of the extent of the error a finite-element model of the Seebeck measurement scheme was implemented with COMSOL Multiphysics. The "Heat transfer in solids" mode was used. A 2-D drawing of the scheme was made and temperatures were measured at the same distances as they are measured with the real device. The error was calculated by comparing the temperature difference at the point probe contacts to the temperature difference at the peltier element and the ceramic support while the heater was set to 3 K higher temperature than the surroundings. The model assumes convection of 10 $W/(m^2K)$ and emissivity of 0.5. The simulated error as a function of the substrate thickness is shown in Figure 4.5. A thin glass substrate is preferred in order to minimize the error, with 0.1 mm glass substrate the error is only 4.8 %. However, in the case of 0.5 mm glass substrate the error is already 18 %. Glass substrate has lower error since it has an order of magnitude larger thermal conductivity than Kapton, yet it would not be beneficial to use even more thermally conductive substrate as it would thermally short circuit the sample. Sustaining a temperature gradient in a thermal conductor is, if not impossible, very unpractical. Thus, the total error for the Seebeck coefficient is about 7.5 % of which 2.5 % is caused by the instrumentation and 5 % by geometry. Worth noting is that the error caused by the geometry is constantly giving lower value for the Seebeck coefficient. Therefore, if the Seebeck coefficient of a thick sample needs to be estimated, the error may be used as a correction factor as well.

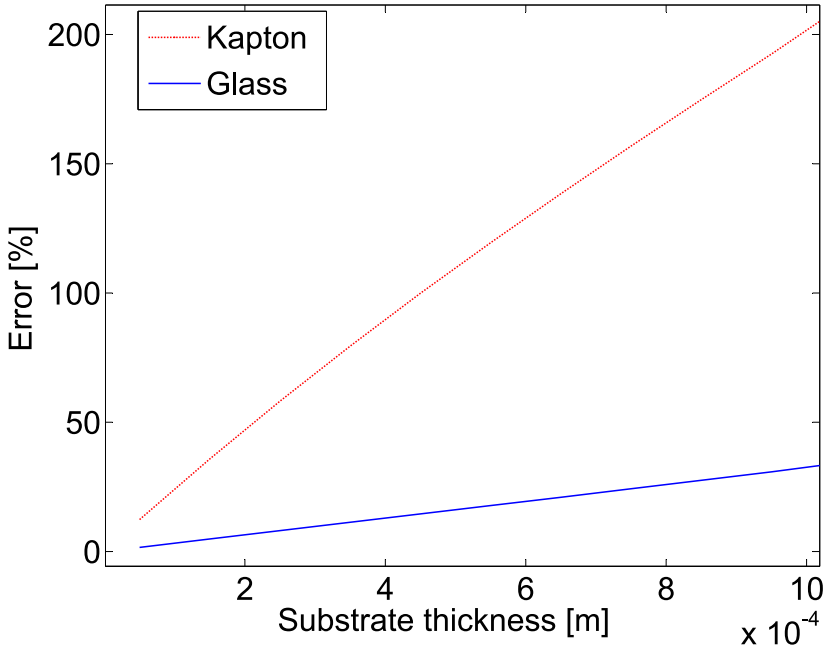

Figure 4.5: Error in the Seebeck coefficient measurement caused by the geometry of voltage and temperature difference measurements.

5 Materials and methods

Atomic layer deposition (ALD) was used to grow ZnO thin films on hydrolytic glass (Gerhard Menzel GmbH, Braunschweig) and fused silica (Corning Incorporated, Corning) substrates in BENEQ TFS-500 ALD reactor. The power factor of the films was characterized with the measurement system described in Section 4.3

Atomic layer deposition is a chemical vapour deposition (CVD) technique, which utilizes sequential pulses of self-terminating gas-solid reactions. The growth of material layers by ALD is done by repeating four steps illustrated in Figure 5.1: 1) Self-terminating reaction of the first reactant and the substrate, 2) removal of non-reacted precursors is typically done with inert gas pulse, 3) self-terminating reaction of the second reactant and monolayer of the first reactant and 4) removal of excess second reactant. The cycles are repeated until desired amount of material is deposited. As ALD is a surface-controlled process, other process parameters than substrate, temperature and reactants have little influence. In addition, the films are very conformal and uniform in thickness. The drawback is that the growth rate is slow, only a few Ångström per cycle.

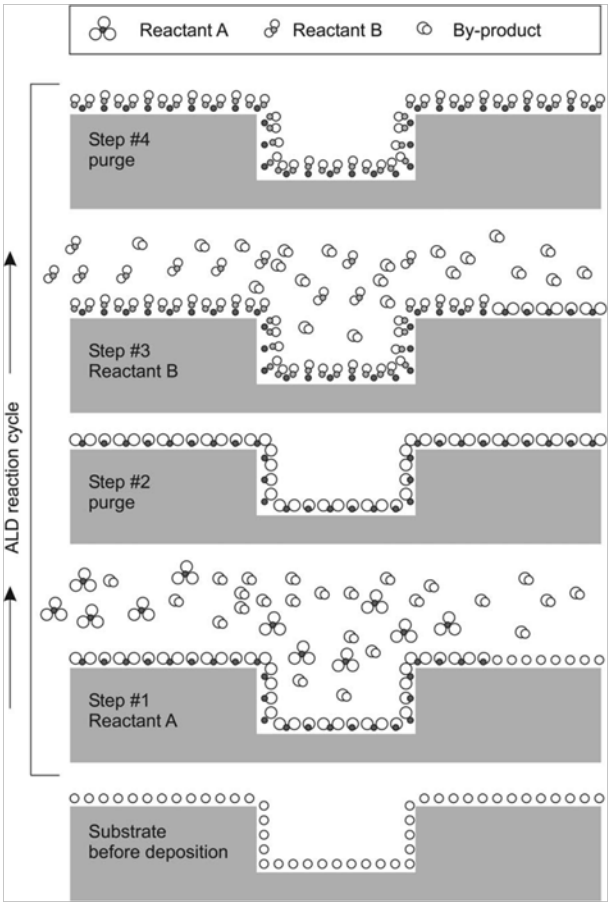

Figure 5.1: Schematic presentation of one ALD cycle [35].

Table 5.1: Parameters.

Name(s) of sample	Thickness (nm)	Growth temperature (^{o}C)	Fraction of TMA cycles (%)	Pulse time (ms)
Sample 1: ZnO:Al	90	200	5	400 ms (DEZ) 250 ms (TMA) 250 ms (H_2O)
Sample 2: ZnO	85	165	0	400 ms (DEZ) 250 ms (H_2O)

ALD growth of ZnO was done by using DEZ (diethylzinc), trimethylaluminium (TMA) and H_2O as precursors. The exact growth parameters for each sample are listed in Table 5.1

Thickness of the films was determined by ellipsometry. The variation of the film thickness was within 1%. Ohmic contacts [36] were evaporated on the thin films by electron gun evaporator at 10^{-6} mbar vacuum. First 10 nm of titanium was evaporated followed by 50 nm gold film deposition. The samples were washed in acetone, isopropanol and deionised water water before the evaporation.

In order to examine the stability of the thin film properties, the samples were annealed in air at temperature of 200 ^{o}C for various durations and remeasured subsequently.

6 Results

The resistivity, Seebeck coefficient and power factor of 90 nm thick ZnO:Al thin film are shown in Figures 6.1, 6.2 and 6.3, respectively. The resistivity values for as deposited samples are consistent with the literature [37]. Seebeck coefficient of the 20 h annealed sample could not be measured since high resistance led to too noisy results.

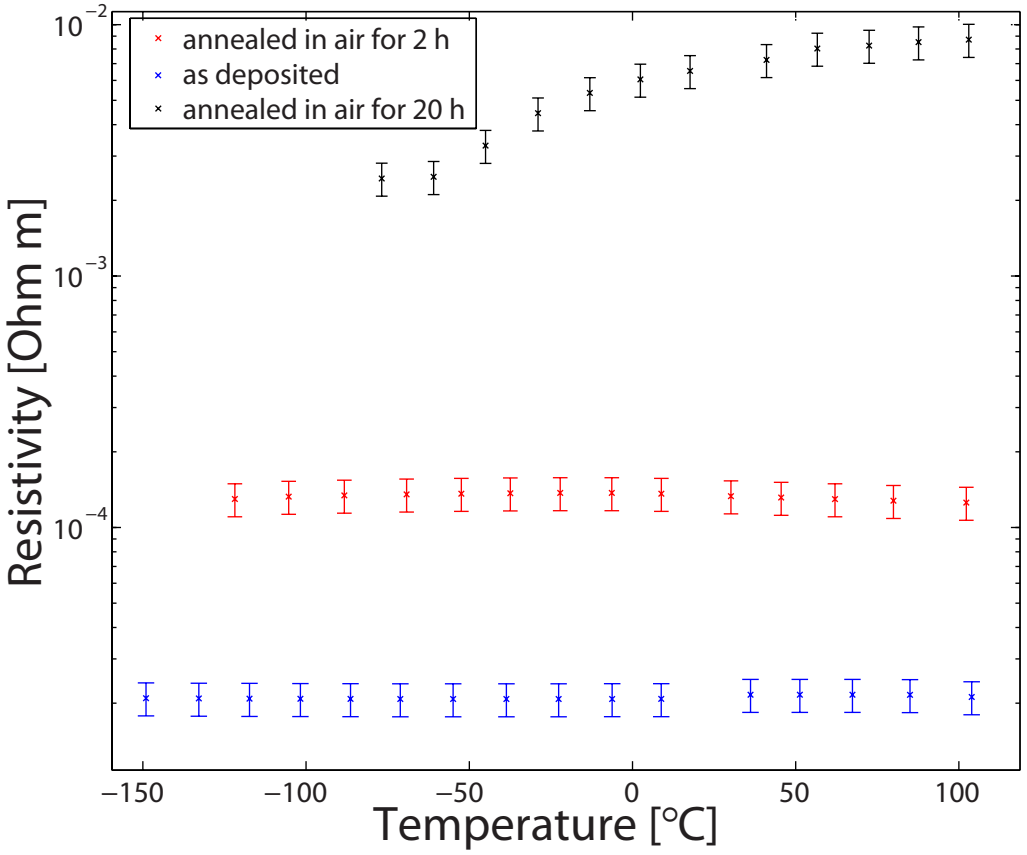

Figure 6.1: Resistivity of ZnO:Al as a function of the temperature.

As can be seen from Figure 6.1, the resistivity has metallic temperature dependence, yet it degraded significantly while high temperature annealing. In other words the material behaves in two different manners depending on the exposure to air. ALD deposition is done in rough vacuum and as a result the film is oxygen deficient. Aluminium has solubility limit of about 0.3 at.% in ZnO, any further Al addition will lead to formation of insulating $ZnAl_2O_4$ phase. As $ZnAl_2O_4$ should not influence charge carrier concentration, the formation of the phase is believed to induce oxygen vacancies. Moreover, formation of one vacancy induces two free electrons, leading

to low resistivity. As the sample is heated in air the vacancies are filled and the charge carrier concentration decreases. This should be reversible. [38]

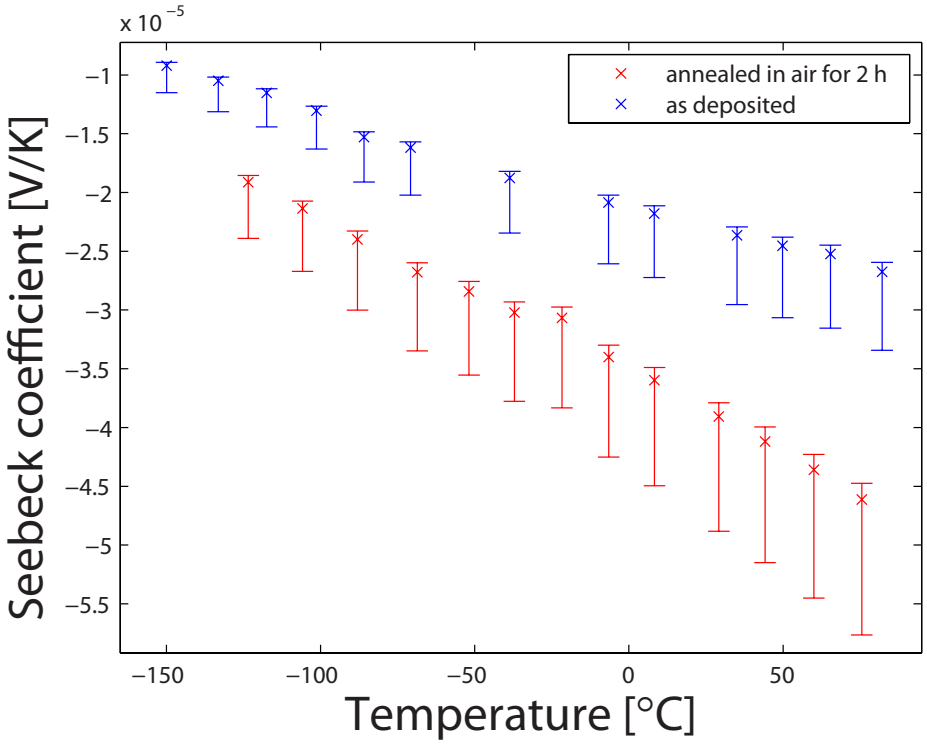

Figure 6.2: Seebeck coefficient of ZnO:Al as a function of the temperature.

However, the resistivity value obtained for 20 h annealed sample is one of the highest values reported for Al-doped ZnO, typically highest values are in the same order as 2 h annealed sample. The reason for this remains so far unknown.

The Seebeck coefficients for ALD deposited Al-doped ZnO have not been previously published, and for ZnO thin films only a few publications exists. For RF sputtered $Zn_{0.97}AL_{0.03}O$ a Seebeck coefficient of -90 $\mu V/K$ was obtained at room temperature, which is significantly higher than reported here, however the resistivity was also an order of magnitude higher, $1.4*10^{-4}$ Ωm [39]. In comparison to bulk ZnO:Al the aluminium doped sample has roughly the same resistivity, but Seebeck coefficient have been reported to go up to -150 $\mu V/K$ [20], although similar values as here have been reported as well [38].

The resistivity, Seebeck coefficient and power factor of 85 nm thick ZnO thin film are shown in Figures 6.4, 6.5 and 6.6, respectively. The sample was also annealed at 200 ^oC for 1 hour, but either the resistivity and the Seebeck coeffcient were not

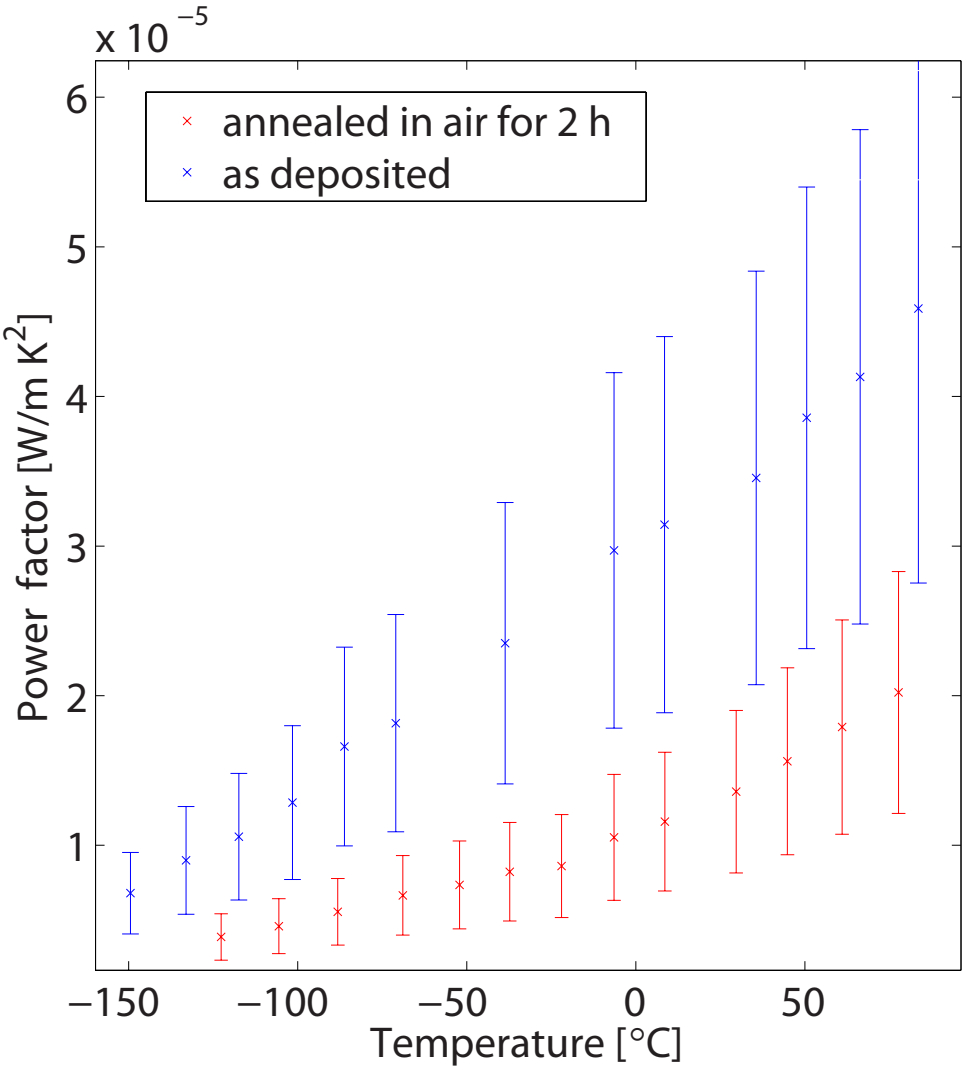

Figure 6.3: Power factor of ZnO:Al as a function of the temperature.

measurable. Consistent values were not obtained due to the large contact potentials. Non-doped ZnO is generally considered as non-conductive semiconductor with Seebeck coefficient up to -300 $\mu V/K$ and resistivity in the order of 0.1 Ωm [20, 38]. However, ALD deposited ZnO behaves metallically with reasonable Seebeck coefficient. Moreover, ALD deposited ZnO seems to be the only system in which non-doped material has better thermoelectric properties than the doped one. However, the materials properties are strongly related to exposure of oxygen at elevated temperatures, which can be seen in Figure 6.4 as heating the sample only to 100 ^oC

increases the resistivity about 30%.

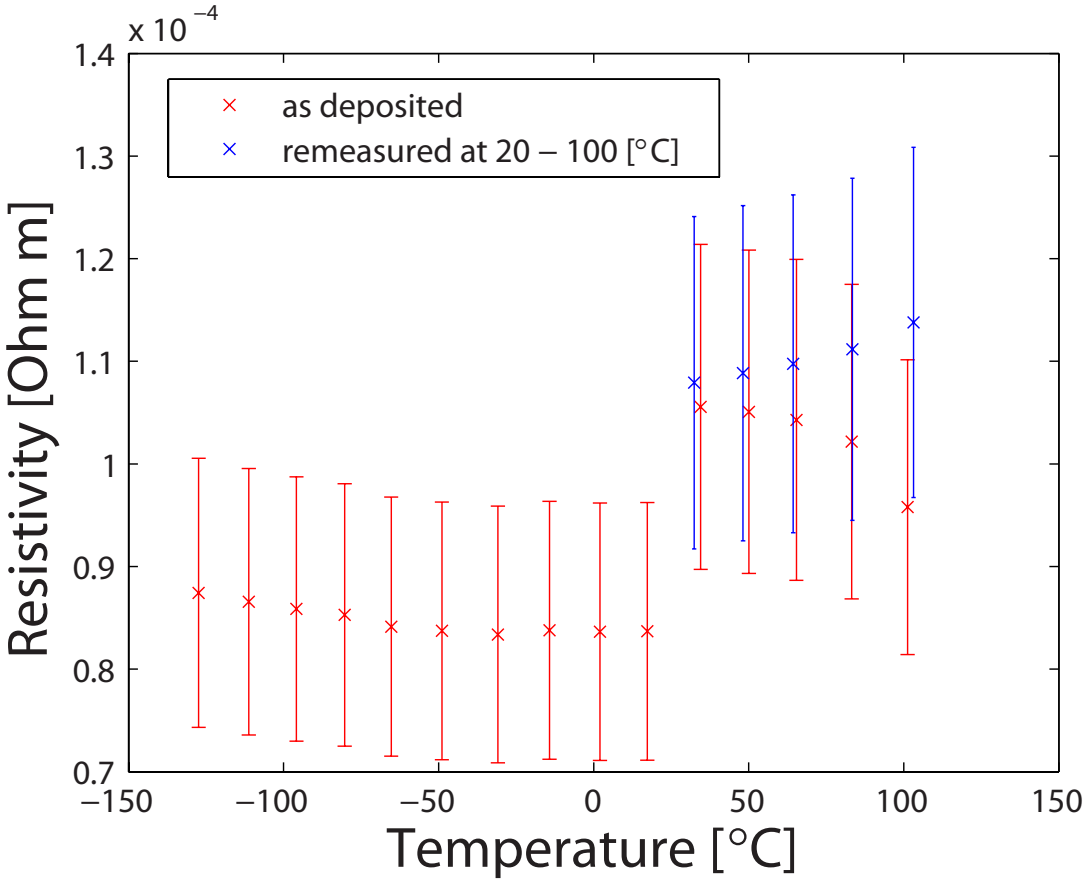

Figure 6.4: Resistivity of ZnO as a function of the temperature.

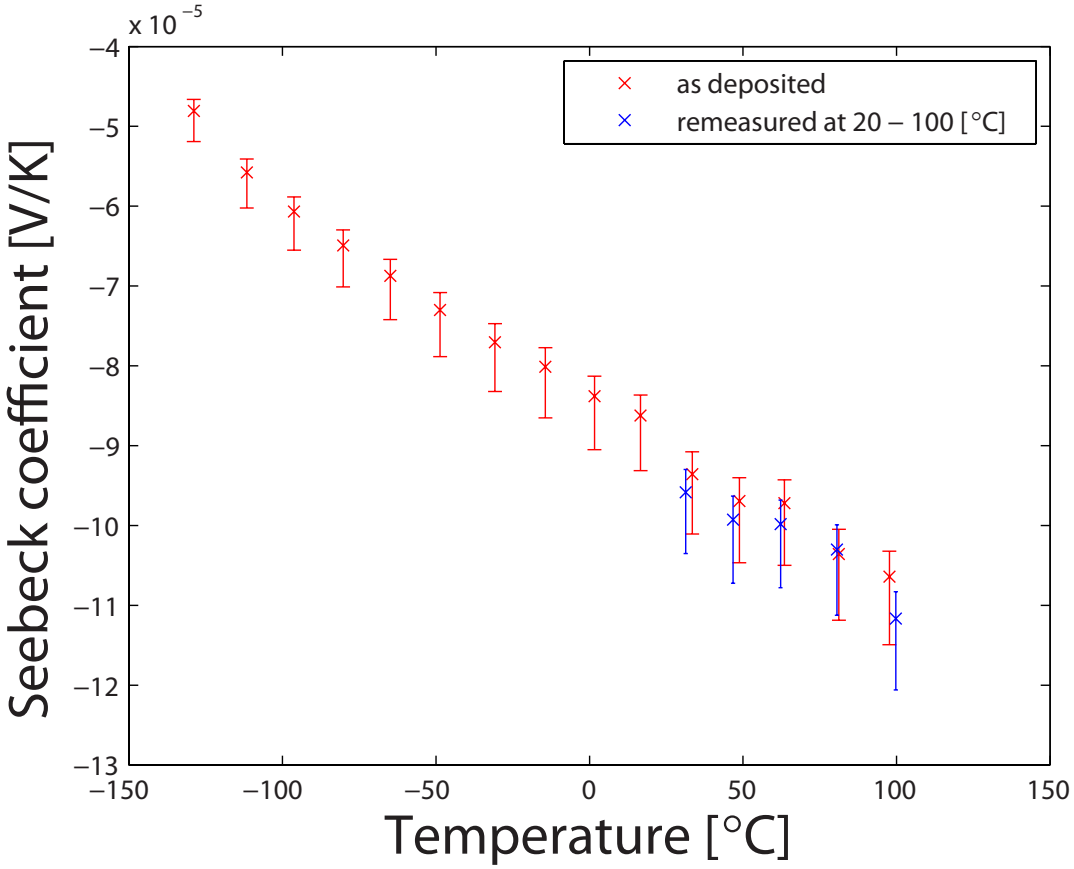

Figure 6.5: Seebeck coefficient of ZnO as a function of the temperature.

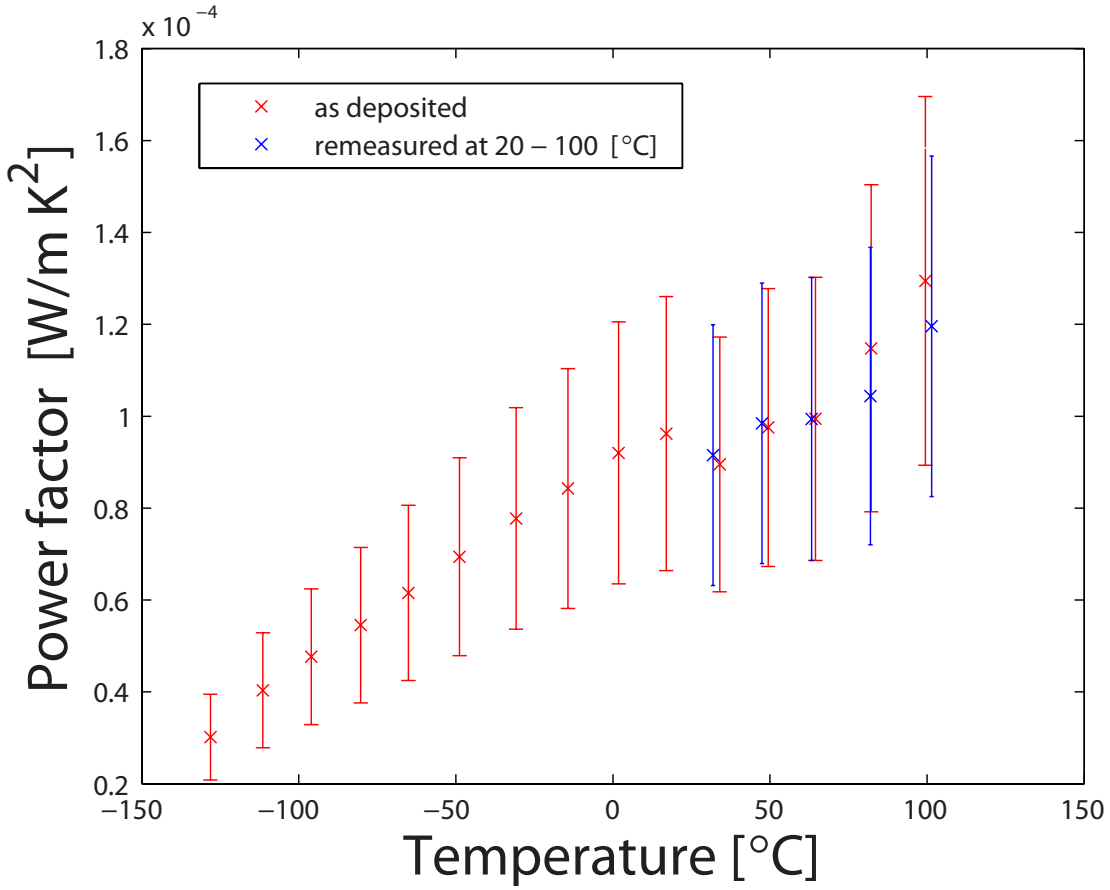

Figure 6.6: Power factor of ZnO as a function of the temperature.

7 Conclusions

This thesis presents the thermoelectric properties of ALD deposited ZnO with and without Al-doping. The results are interesting in comparison to bulk ZnO, yet the low resistivity of ALD deposited ZnO have been known for many years. Moreover, the strong dependence of oxygen stoichiometry to the film properties is well known phenomenon, yet the exact mechanism is still unclear [18]. Hence, further investigations are needed to clarify the dependence of various growth conditions and doping on ZnO properties and with subsequent heat treatments. In addition, XRD studies would yield valuable information on the phases and doping levels in the material. With Hall measurements these changes could be linked to number of charge carriers and their mobility.

Based on the work presented in the thesis, it impossible to present ZnO as reliable engineering material. In order to use it at elevated temperatures, various oxygen barriers have to be implemented in order to stabilize the materials properties.

The measurement device presented in this thesis is a tool for material optimization rather than precision scientific instrument. The whole design of the device was optimized for fast sample exchangeability and automation. The time required from the operator to measure a sample lies in about 30 minutes, although the measurement takes about 10 hours. The validity of the data is still somewhat unclear. There is a need to compare the results obtained with the ones measured with other similar devices.

This thesis discussed the means to improve thermoelectric conversion efficiency and took the initial steps to realize them. ALD is a powerful tool for coating nanoscale structures with atomic layer precision. The real challenges with nanoscale objects in the thermoelectric research are, however, the measurements. An idea of having a device to measure them is impossible; good enough thermal and electrical contacts would likely never be achieved. The only way to overcome this hurdle is to incorporate the contacts with the nanostructure by design.

References

[1] Elliott, S. R. *The physics and chemistry of solids.* Chichester, Wiley, 1998.

[2] Foll, H. Thermoelectric effects. Web document. Referenced 16.12.2010. Available: http://www.tf.uni-kiel.de/matwis/amat/elmat_en/ka_2/advanced/t2_3_2.html.

[3] Rowe, D. M. *Thermoelectrics handbook macro to nano.* Boca Raton, CRC/Taylor & Francis, 2006.

[4] Goldsmid, H.J. *Introduction to thermoelectricity.* Heidelberg, Springer Verlag, 2009.

[5] Rockwood, A.L. *Relationship of thermoelectricity to electronic entropy.* Physical Review A, Vol. 30, Issue 5, pp. 2843-2844, 1984.

[6] Snyder, G.J. and Toberer, E.S. *Complex thermoelectric materials.* Nature Materials, Vol. 7, Issue 2, pp. 105-114, 2008. DOI: 10.1038/nmat2090.

[7] Narducci, D. *Do we really need high thermoelectric figures of merit? A critical appraisal to the power conversion efficiency of thermoelectric materials.* Applied Physics Letters, Vol. 99, Issue 10, pp. 102104, 2011. DOI: 10.1063/1.3634018.

[8] Rowe, D.M. and Min, G. *α-ln σ plot as a thermoelectric material performance indicator.* Journal of Materials Science Letters, Vol. 14, Issue 9, pp. 617-619, 1995. DOI: 10.1007/BF00586157.

[9] Vaqueiro, P. and Powell, A.V. *Recent developments in nanostructured materials for high-performance thermoelectrics.* Journal of Materials Chemistry, Vol. 20, Issue 43, pp. 9577-9584, 2010. DOI: 10.1039/C0JM01193B

[10] H J Goldsmid and, R.W.D. *The use of semiconductors in thermoelectric refrigeration.* British Journal of Applied Physics, Vol. 5, Issue 11, pp. 386, 1954.

[11] Sootsman, J., Chung, D. and Kanatzidis, M. *New and Old Concepts in Thermoelectric Materials.* Angewandte Chemie International Edition, Vol. 48, Issue 46, pp. 8616-8639, 2009. DOI: 10.1002/anie.200900598.

[12] Nolas, G.S., Sharp, J., Goldsmid, H.J. *Thermoelectrics : basic principles and new materials developments.* Berlin ; London, Springer, 2001.

[13] Mishra, S.K., Satpathy, J. and Jepsen, O. *Electronic structure and thermoelectric properties of bismuth telluride and bismuth selenide.* Journal of Physics: Condensed Matter, Vol. 9, Issue 2, pp. 461, 1997. DOI:10.1088/0953-8984/9/2/014

[14] Venkatasubramanian, R., Siivola, E., Colpitts, T. and O'Quinn, B. *Thin-film thermoelectric devices with high room-temperature figures of merit.* Nature, Vol. 413, Issue 6856, pp. 597-602, 2001. DOI: 10.1038/35098012

[15] Dughaish, Z.H. *Lead telluride as a thermoelectric material for thermoelectric power generation.* Physica B: Condensed Matter, Vol. 322, Issue 1-2, pp. 205-223, 2002. DOI: 10.1016/S0921-4526(02)01187-0.

[16] European Synchrotron Radiation Facility Element Specific Vibrational Dynamics in Filled Skutterudites. Web document. Referenced 19.12.2011. Available: http://www.esrf.eu/UsersAndScience/Publications/Highlights/2005/HRRS/HRRS14

[17] Androulakis, J., Hsu, K.F., Pcionek, R., et al. *Nanostructuring and High Thermoelectric Efficiency in p-Type* $Ag(Pb_{1-y}Sn_y)_mSbTe_{2+m}$. Advanced Materials, Vol. 18, Issue 9, pp. 1170-1173, 2006. DOI: 10.1002/adma.200502770.

[18] Özgür, Ü., Alivov, Y.I., Liu, C., et al. *A comprehensive review of ZnO materials and devices.* Journal of Applied Physics, Vol. 98, Issue 4, pp. 041301-103, 2005. DOI: 10.1063/1.1992666.

[19] Ohtaki, M., Yamamoto, K., and Iwano, Y. *Thermoelectric Properties of ZnO with Multinary Doping.* The 30th International Conference on Thermoelectrics July 17-21, 2011

[20] Ohtaki, M., Tsubota, T., Eguchi, K. and Arai, H. *High-temperature thermoelectric properties of (Zn1-xAlx)O.* Journal of Applied Physics, Vol. 79, Issue 3, pp. 1816-1818, 1996.

[21] Tanaka, Y., Ifuku, T., Tsuchida, K. and Kato, A. *Thermoelectric properties of ZnO-based materials.* Journal of Materials Science Letters, Vol. 16, Issue 2, pp. 155-157, 1997. DOI: 10.1023/A:1018506430036.

[22] Pichanusakorn, P. and Bandaru, P. *Nanostructured thermoelectrics.* Materials Science and Engineering: R: Reports, Vol. 67, Issue 2-4, pp. 19-63, 2010. DOI: 10.1016/j.mser.2009.10.001.

[23] Harrison A., H. *Solid state theory* New York, McGraw-Hill, 1970.

[24] Boukai, A.I., Bunimovich, Y., Tahir-Kheli, J., Yu, J., Goddard III, W.A. and Heath, J.R. *Silicon nanowires as efficient thermoelectric materials.* Nature, Vol. 451, Issue 7175, pp. 168-171, 2008. DOI: 10.1038/nature06458

[25] Swartz, E.T. and Pohl, R.O. *Thermal boundary resistance.* Reviews of Modern Physics, Vol. 61, Issue 3, pp. 605, 1989. DOI: 10.1103/RevModPhys.61.605

[26] Pennec, Y., Vasseur, J.O., Djafari-Rouhani, B., Dobrzyn'ski, L. and Deymier, P.A. *Two-dimensional phononic crystals: Examples and applications.* Surface Science Reports, Vol. 65, Issue 8, pp. 229-291, 2010. DOI: 10.1016/j.surfrep.2010.08.002.

[27] Heremans, J.P., Jovovic, V., Toberer, E.S., et al. *Enhancement of Thermoelectric Efficiency in PbTe by Distortion of the Electronic Density of States.* Science, Vol. 321, Issue 5888, pp. 554-557, 2008. DOI: 10.1126/science.1159725.

[28] Mahan, G.D. and Sofo, J.O. *The best thermoelectric.* Proceedings of the National Academy of Sciences, Vol. 93, Issue 15, pp. 7436-7439, 1996.

[29] Snyder, G.J. *PbTe - Better Than We Thought.* The 30th International Conference on Thermoelectrics July 17-21, 2011

[30] Martin, J., Tritt, T. and Uher, C. *High temperature Seebeck coefficient metrology.* Journal of Applied Physics, Vol. 108, Issue 12, pp. 121101-12, 2010. DOI: 10.1063/1.3503505.

[31] Werheit, H., Kuhlmann, U., Herstell, B., and Winkelbauer, W. *Reliable measurement of Seebeck coefficient in semiconductors.* Journal of Physics: Conference Series, Vol. 176, Issue 1, pp. 012037, 2009. DOI: 10.1088/1742-6596/176/1/012037

[32] Iwanaga, S., Toberer, E.S., LaLonde, A. and Snyder, G.J. *A high temperature apparatus for measurement of the Seebeck coefficient.* Review of Scientific Instruments, Vol. 82, Issue 6, pp. 063905-6, 2011. DOI: 10.1063/1.3601358.

[33] Smits, F.M., *Measurement of sheet resistivities with the four-point probe.* Bell System Technical Journal, 711, 1958.

[34] van der Pauw, L.J., *A method of measuring specific resistivity and Hall effect of discs of arbitrary shape.* Philips Research Reports, 13, 1, 1958.

[35] Puurunen, R. *Surface chemistry of atomic layer deposition: A case study for the trimethylaluminum/water process.* Journal of Applied Physics, Vol. 97, Issue 12, pp. 121301, 2005. DOI: 10.1063/1.1940727.

[36] Kim, H., Han, S., Seong, T. and Choi, W. *Low-resistance Ti/Au ohmic contacts to Al-doped ZnO layers.* Applied Physics Letters, Vol. 77, Issue 11, pp. 1647-1649, 2000. DOI: 10.1063/1.1308527.

[37] Ritala, M., Asikainen, T., Leskela, M. and Skarp, J. *Ale growth of transparent conductors.* Materials Research Society Symposium Proceedings: Thin Films for Photovoltaic and Related Device Applications, Vol. 426, pp. 513-518, 1996.

[38] Bérardan, D., Byl, C. and Dragoe, N. *Influence of the Preparation Conditions on the Thermoelectric Properties of Al-Doped ZnO.* Journal of the American Ceramic Society, Vol. 93, Issue 8, pp. 2352-2358, 2010. DOI: 10.1111/j.1551-2916.2010.03751.x.

[39] Teehan, S., Efstathiadis, H. and Haldar, P. *Enhanced power factor of Indium co-doped ZnO:Al thin films deposited by RF sputtering for high temperature thermoelectrics.* Journal of Alloys and Compounds, Vol. 509, Issue 3, pp. 1094-1098, 2011. DOI: 10.1016/j.jallcom.2010.10.004.